Monthly Notices of the ROYAL ASTRONOMICAL SOCIETY

MNRAS **527,** 11138–11157 (2024) https://doi.org/10.1093/mnras/stad3837
Advance Access publication 2023 December 13

TOI-544 b: a potential water-world inside the radius valley in a two-planet system

H. L. M. Osborne [1,2★] V. Van Eylen [1] E. Goffo,[3,4] D. Gandolfi [3] G. Nowak [5,6,7] C. M. Persson,[8] J. Livingston [9,10,11] A. Weeks,[1] E. Pallé,[6,7] R. Luque [12] C. Hellier,[13] I. Carleo,[6] S. Redfield,[14] T. Hirano,[9,10,11] M. Garbaccio Gili,[3] J. Alarcon,[15] O. Barragán,[16] N. Casasayas-Barris,[6,7] M. R. Díaz,[17] M. Esposito,[4] E. Knudstrup,[18] J. S. Jenkins,[19,20] F. Murgas,[6,7] J. Orell-Miquel,[6,7] F. Rodler,[15] L. Serrano,[3] M. Stangret,[6,7] S. H. Albrecht,[18] A. Alqasim,[1] W. D. Cochran,[21] H. J. Deeg,[12,22] M. Fridlund,[8,23] A. P. Hatzes,[4] J. Korth[24] and K. W. F. Lam[25]

[1]*Mullard Space Science Laboratory, University College London, Holmbury St Mary, Dorking, Surrey RH5 6NT, UK*
[2]*European Southern Observatory, Karl-Schwarzschild-Straße 2, D-85748 Garching bei München, Germany*
[3]*Dipartimento di Fisica, Universitá di Torino, via P. Giuria 1, I-10125 Torino, Italy*
[4]*Thüringer Landessternwarte Tautenburg, Sternwarte 5, D-07778 Tautenburg, Germany*
[5]*Institute of Astronomy, Faculty of Physics, Astronomy and Informatics, Nicolaus Copernicus University, Grudziądzka 5, PL-87-100 Toruń, Poland*
[6]*Instituto de Astrofísica de Canarias (IAC), c/ Via Lactea, s/n, E-38205 La Laguna, Tenerife, Spain*
[7]*Departamento de Astrofísica, Universidad de La Laguna (ULL), E-38206 La Laguna, Tenerife, Spain*
[8]*Department of Space, Earth and Environment, Chalmers University of Technology, Onsala Space Observatory, SE-439 92 Onsala, Sweden*
[9]*Astrobiology Center, 2-21-1 Osawa, Mitaka, Tokyo 181-8588, Japan*
[10]*National Astronomical Observatory of Japan, 2-21-1 Osawa, Mitaka, Tokyo 181-8588, Japan*
[11]*Department of Astronomy, The Graduate University for Advanced Studies (SOKENDAI), 2-21-1 Osawa, Mitaka, Tokyo, 181-8588 Japan*
[12]*Department of Astronomy and Astrophysics, University of Chicago, Chicago, IL 60637, USA*
[13]*Astrophysics Group, Keele University, Staffordshire ST5 5BG, UK*
[14]*Astronomy Department and Van Vleck Observatory, Wesleyan University, Middletown, CT 06459, USA*
[15]*European Southern Observatory, Alonso de Cordova 3107, 7630391 Vitacura, Santiago de Chile, Chile*
[16]*Sub-department of Astrophysics, Department of Physics, University of Oxford, Oxford OX1 3RH, UK*
[17]*Las Campanas Observatory, Carnegie Institution of Washington, Colina el Pino, Casilla 601, La Serena, Chile*
[18]*Stellar Astrophysics Centre, Department of Physics and Astronomy, Aarhus University, Ny Munkegade 120, DK-8000 Aarhus C, Denmark*
[19]*Instituto de Astrofísica de Andalucía (IAA-CSIC), Glorieta de la Astronomía s/n, E-18008 Granada, Spain*
[20]*Centro de Astrofísica y Tecnologías Afines (CATA), Casilla 36-D, Santiago, 7591245 Chile*
[21]*McDonald Observatory and Center for Planetary Systems Habitability, The University of Texas TX 78712-1206, Austin, Texas, USA*
[22]*Instituto de Estudios Astrofísicos, Facultad de Ingeniería y Ciencias, Universidad Diego Portales, Av. Ejército 441, Santiago, Chile*
[23]*Leiden Observatory, University of Leiden, PO Box 9513, NL-2300 RA Leiden, The Netherlands*
[24]*Lund Observatory, Division of Astrophysics, Department of Physics, Lund University, Box 43, SE-22100 Lund, Sweden*
[25]*Institute of Planetary Research, German Aerospace Center (DLR), Rutherfordstrasse 2, D-12489 Berlin, Germany*

Accepted 2023 December 6. Received 2023 December 1; in original form 2023 May 16

ABSTRACT

We report on the precise radial velocity follow-up of TOI-544 (HD 290498), a bright K star ($V = 10.8$), which hosts a small transiting planet recently discovered by the *Transiting Exoplanet Survey Satellite (TESS)*. We collected 122 high-resolution High Accuracy Radial velocity Planet Searcher (HARPS) and HARPS-N spectra to spectroscopically confirm the transiting planet and measure its mass. The nearly 3-yr baseline of our follow-up allowed us to unveil the presence of an additional, non-transiting, longer-period companion planet. We derived a radius and mass for the inner planet, TOI-544 b, of 2.018 ± 0.076 $R_\oplus$ and 2.89 ± 0.48 $M_\oplus$, respectively, which gives a bulk density of $1.93^{+0.30}_{-0.25}$ g cm^{-3}. TOI-544 c has a minimum mass of 21.5 ± 2.0 $M_\oplus$ and orbital period of 50.1 ± 0.2 d. The low density of planet-b implies that it has either an Earth-like rocky core with a hydrogen atmosphere, or a composition which harbours a significant fraction of water. The composition interpretation is degenerate depending on the specific choice of planet interior models used. Additionally, TOI-544 b has an orbital period of 1.55 d and equilibrium temperature of 999 ± 14 K, placing it within the predicted location of the radius valley, where few planets are expected. TOI-544 b is a top target for future atmospheric observations, for example with *JWST*, which would enable better constraints of the planet composition.

Key words: techniques: radial velocities – planets and satellites: composition – planets and satellites: detection.

★ E-mail: hannah.osborne.19@ucl.ac.uk

1 INTRODUCTION

The radius valley describes the region in the size distribution of exoplanets where few planets exist, specifically between 1.5 and 2.0 $R_\oplus$. This feature was first observationally identified in Fulton et al. (2017) and Van Eylen et al. (2018) and a variety of theories have been proposed to explain this gap in planetary radii, including photo-evaporation (Fulton et al. 2017; Owen & Wu 2017; Van Eylen et al. 2018) and core-powered mass-loss (Collier Cameron & Jardine 2018; Gupta & Schlichting 2019, 2021). Photo-evaporation models argue that planets generally form with rocky cores and atmospheric layers composed of hydrogen and helium (H–He) of around 1 per cent by mass. Such planets, with a rocky core and H–He atmosphere, are termed sub-Neptunes and located above the radius valley in radius-period space. In some cases, the intense X-ray flux from the nearby host star strips away these volatile gases, leaving behind a bare rocky core, a so-called super-Earth planet, with a radius placing it below the radius valley (Owen & Wu 2017). Core-powered mass-loss models are similar in that they predict planets to form with atmospheric layers and be located above the valley and subsequent atmospheric loss reduces the radius and locates the planet below the valley. In the latter model, the energy enabling the mass-loss has come from within the planet itself; stored heat from the formation of the planet escapes from the core and heats the atmospheric layer from the inside, leading to gaseous escape (Gupta & Schlichting 2019). Despite several attempts (e.g. Owen & Wu 2017; Lopez & Rice 2018; Gupta & Schlichting 2019; Estrela et al. 2020; Gupta, Nicholson & Schlichting 2022; Ho & Van Eylen 2023) no significant observational evidence has been found that can differentiate between models. There is also an additional complication in the fact that the location of the radius valley seems to change based on other parameters, in particular on stellar mass (see e.g. Petigura et al. 2022). Cloutier & Menou (2020) calculated the occurrence rates of small planets orbiting low-mass stars to show that the location of the radius valley shifts to smaller sizes for decreasing stellar mass. They also argue that for planets around lower mass stars the radius valley may have a different formation mechanism or mechanisms, and highlight the need for high-precision radial velocity (RV) follow-up of a number of key targets including TOI-544 b.

Additionally, recent works have suggested that the observed distribution of small planets (particularly those orbiting M-dwarf stars) is the result of a distribution in core composition at formation. Specifically, Luque & Pallé (2022) argue that the small planets around M-dwarfs can be separated into super-Earths (with rocky cores) and water worlds (with large fractions of ice or water layers). Other recent detections have also seemed to provide evidence towards this divergence in core compositions. Piaulet et al. (2022) presents a detailed study of Kepler-138 d, a small planet with a bulk density which they argue can only be explained with a water world composition (see also e.g. Cadieux et al. 2022; Diamond-Lowe et al. 2022). However, Rogers, Schlichting & Owen (2023) use models which include atmospheric boil-off shortly after planet formation to show that the group of water-world planets presented in Luque & Pallé (2022) are consistent with atmospheric loss models where a rocky planet with a H–He atmosphere loses its atmospheric layers to become a stripped core.

In this context, we have performed follow-up high-resolution RV observations within the KESPRINT consortium[1] of the small planet TOI-544 b discovered by the Transiting Exoplanet Survey Satellite (*TESS*; Ricker et al. 2014). The planet is particularly interesting since it is located in the middle of the radius valley and has a short period of 1.5 days. It was recently validated by Giacalone et al. (2022), where they present observations from the *TESS* follow-up programme, who argued that TOI-544 b is a potentially interesting target for *JWST*.

In Section 2, we present the space-based and ground-based observations of TOI-544, including the extensive RV measurements. In Section 3, we describe our stellar parameter fitting method and results. In Section 4, we describe both the transit fitting and the RV fitting and in Sections 5.1 to 5.4 we explore the composition of the inner planet, its location in relation to the radius valley and potential atmospheric observations of this planet. Finally, we present conclusions in Section 6.

2 OBSERVATIONS

2.1 Space-based photometry

As part of its all-sky survey, *TESS* observed the star TIC 50 618 703 in Sectors 6 and 32. The cadence of observations is 120 s, the time span of Sector 6 (32) is 2018 December 12 to 2019 January 06 (2020 November 19 to 2020 December 16), and 44/14691 (817/17977) cadences were omitted due to bad quality flags in Sector 6 (32). After data reduction though the standard Science Processing Operations Centre (SPOC; Jenkins et al. 2016; Twicken et al. 2019) pipeline, likely transits were detected and the planetary candidate was promoted to a *TESS* object of interest (TOI), named TOI-544, by the *TESS* team. *TESS* observations of TOI-544 are shown in Fig. 1.

2.2 Ground-based photometry

Prior to the initial planet detection by *TESS*, the Wide Angle Search for Planets (WASP) survey (Pollacco et al. 2006) observed the field of TOI-544 between 2008 and 2011, obtaining 18 000 photometric data points using Canon 200-mm, f/1.8 lenses with a 400–700 nm filter and CCDs with a plate scale of 13.7 arcsec per pixel. The data have a typical 15-min cadence and covered an observing season of $\sim$ 100 nights in each year. TOI-544 is by far the brightest star in the 48-arcsec extraction aperture, with a V magnitude of 10.777 ± 0.017. We make use of this archival data by searching the resulting WASP light curves for a stellar rotational modulation, adopting the methods described in Maxted et al. (2011a). We find a significant modulation at a period of 20 ± 1 d and an amplitude of up to 3 mmag. In the combined data set the modulation is significant to a level of >99 per cent confidence. Fig. 2 shows Generalized Lomb–Scargle periodograms, adapted as described in Maxted et al. (2011b), of the WASP data for TOI-544. The 1 per cent false-alarm probability is shown by the horizontal line and the panels to the right show the data folded on the 20 d rotation period.

2.3 High-resolution HARPS and HARPS-N spectroscopy

We obtained a total of 108 high-resolution ($R = \lambda/\Delta\lambda \approx 115\,000$) spectroscopic observations of TOI-544 using the High Accuracy Radial velocity Planet Searcher (HARPS) mounted on the European Southern Observatory (ESO) 3.6-m telescope at La Silla Observatory. One hundred and six spectra were acquired between December 2020 and March 2022 as part of our large observing programme 106.21TJ.001 (PI: Gandolfi). There are additional 2 observations taken during 2019 April as part of observing programme 0103.C-0442(A) (PI: Diaz). Each observation has an exposure time between

[1] https://kesprint.science

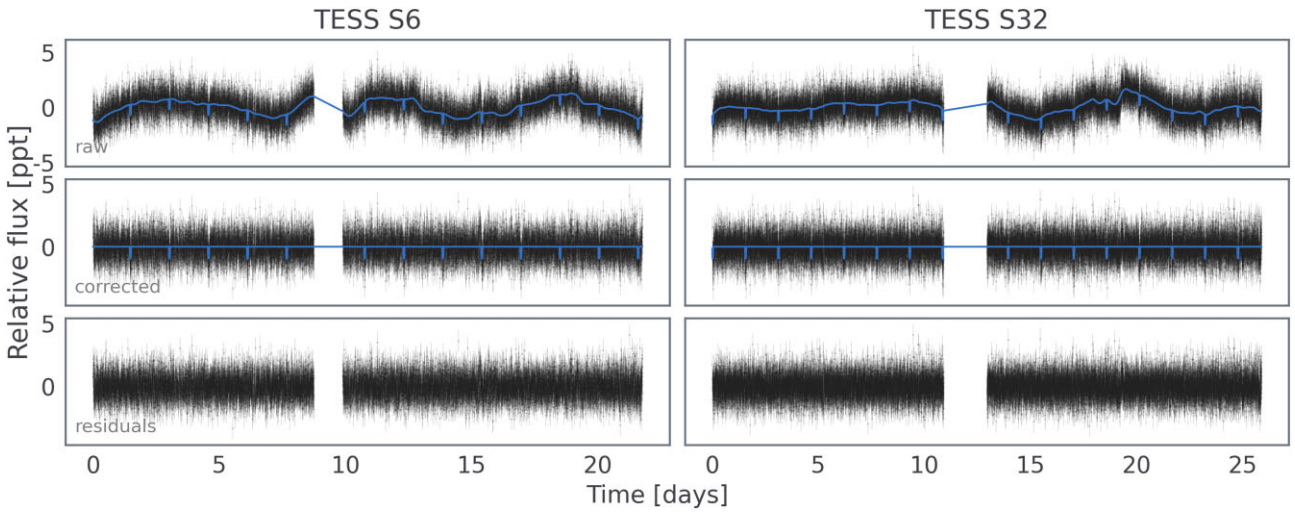

Figure 1. *TESS* light curves from Sector 6 (left) and 32 (right). SPOC light curves are shown in the upper panel, with a full transit and noise model (see Section 4.1) shown in blue. In the middle panel, TESS light curves are shown after subtracting the best-fitting GP model, and residuals are shown in the bottom row.

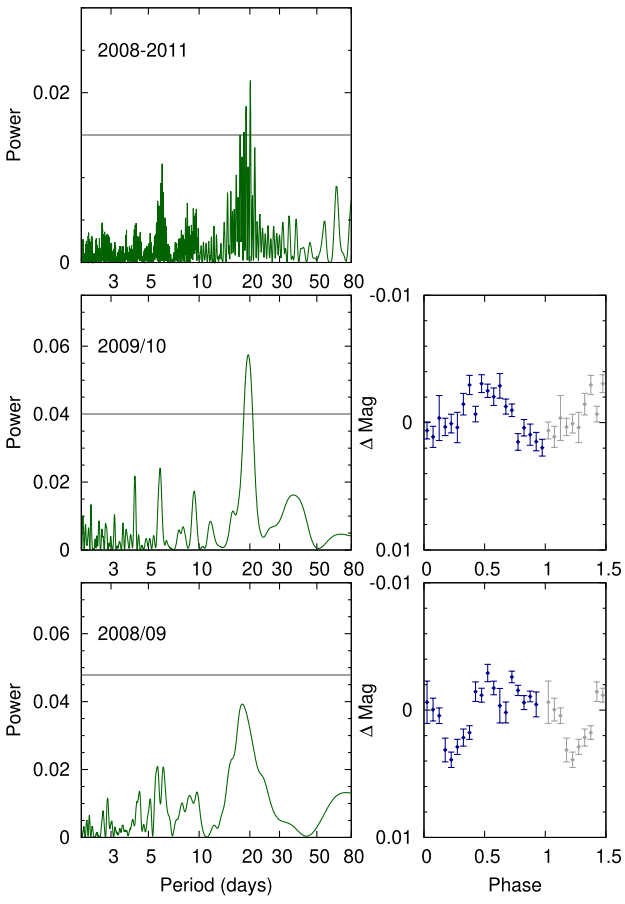

Figure 2. Generalized Lomb–Scargle Periodograms of the WASP-South data for TOI-544. The horizontal line is the estimated 1 per cent false-alarm probability, data after phase 0.5 are in grey. The right-hand panels show the data folded on the 20-d rotational period.

1500 and 2700 s, leading to a median signal-to-noise (S/N) ratio of 53.7 per pixe at 550 nm (Table A1), and a median RV uncertainty of $\sim$1.6 m s^{-1}, as extracted using the SpEctrum Radial Velocity Analyser SERVAL (see below Table A2).

TOI-544 was also observed using the High Accuracy Radial velocity Planet Searcher for the Northern hemisphere (HARPS-N; Cosentino et al. 2012) mounted at the 3.58-m Telescopio Nazionale Galileo of Roque de los Muchachos Observatory in La Palma, Spain, between 2019 April and 2020 December, resulting in a total of 14 high-resolution ($R \approx 115\,000$) spectra from programmes CAT19A_162 and CAT19A_97 (PIs: Nowak and Casasayas-Barris). Each observation has an exposure time between 1230 and 2400 s, a median S/N ratio of 52 per pixel at 550 nm (Table A3), and a median RV precision of $\sim$1.2 m s^{-1}, as extracted using SERVAL (see below; Table A4). We include these 14 observations in our RV analysis. The total number of HARPS and HARPS-N spectra is thus 122.

Versions 3.8 and 3.7 of the Data Reduction Software (DRS; Pepe et al. 2002; Lovis & Pepe 2007) were used to reduce the HARPS and HARPS-N spectra, respectively, and extract absolute RVs by cross-correlating the spectra with a K5 numerical mask (Baranne et al. 1996), along with three diagnostics of the cross-correlation function (CCF), namely, the full width at half-maximum (FWHM), the bisector inverse slope (BIS), and the contrast. We also used the SERVAL code (Zechmeister et al. 2018) to measure relative RVs and extract two additional activity diagnostics, namely, the differential line width (dLW) and the chromatic index (CRX). SERVAL implements a template-matching algorithm that is suitable to derive precise Doppler measurements for M- and late K-type stars when compared to the CCF technique employed by the DRS (see e.g. Luque et al. 2021; Serrano et al. 2022; Goffo et al. 2023).

We finally extracted the Hα, Na D1 & D2, and Ca II S-index activity indicators using the Template Enhanced Radial velocity Re-analysis Application (TERRA; Anglada-Escudé & Butler 2012). The standard deviation of the RV data is $\sim$7.5 m s^{-1} for HARPS and HARPS-N and in both cases of using the SERVAL and DRS codes. The absolute (DRS) and relative (SERVAL) RV measurements are given in

Appendix A, along with the stellar activity indicators and line profile diagnostics. For the analysis presented in Sections 4.2 and 4.3 we used the SERVAL RV measurements due to the lower jitter terms and root-mean-square of the fit residuals with respect to the DRS RVs.

3 STELLAR PARAMETERS

Stellar parameters for TOI-544 were calculated using BASTA (Aguirre Børsen-Koch et al. 2022) run on the co-added HARPS spectra, as follows. First, *Gaia* magnitude G, RA, DEC, and Parallax ϖ were taken from *Gaia* Data Release 3 (DR3; Gaia Collaboration 2021). $T_{\rm eff}$ and [Fe/H] were determined using the empirical software SPECMATCH-EMP (Yee, Petigura & von Braun 2017) which compares the observed data to a library of FGKM stars. We also compared the SPEC-MATCH-EMP results with SME[2] (Spectroscopy Made Easy; Valenti & Piskunov 1996; Piskunov & Valenti 2017). SME computes synthetic spectra with line data from the Vienna atomic line database (VALD)[3] (Ryabchikova et al. 2015) and a chosen stellar atmosphere grid, in our case Atlas12 (Kurucz 2013), which is fitted to the observed spectra. The macro- and micro-turbulent velocities, $V_{\rm mac}$ and $V_{\rm mic}$, were held fixed to 1.5 and 0.5 km s^{-1}, respectively (Gray 2008). A more detailed description of the modelling procedure can be found in Fridlund et al. (2017) and Persson et al. (2018). The results were in very good agreement with SPECMATCH-EMP within 1σ. Table 1 gives the spectroscopic parameters for TOI-544 modelled with SME and SPECMATCH-EMP, we select the parameters using (SPECMATCH-EMP) for our modelling of stellar mass and radius.

An age and metallicity independent prior was placed on stellar mass following the standard Salpeter Initial Mass Function, and reddening and dust were accounted for using the `Bayestar' dustmap (Green et al. 2019). A prior was also set for [Fe/H] allowing for the parameter space to be searched only within an absolute tolerance range of 0.5 dex of the input value. For the isochrones, we used the latest version of BASTI (BAg of STellar Isochrones; Hidalgo et al. 2018), set to the 'Diffusion' science case, described in Pietrinferni et al. (2021), to account for diffusion processes in low-mass stars.

BASTA determines model-dependent parameters using a Bayesian approach, detailed in Silva Aguirre et al. (2015) and following the formalism of Serenelli et al. (2013).

We also used the Python `isochrones` (Morton 2015) interface to the MESA (Modules for Experiments in Stellar Astrophysics) Isochrones and Stellar Tracks (MIST) stellar evolution models (Choi et al. 2016) using the same inputs as for basta, which resulted in very good agreement for the stellar mass and radius (within $\sim 0.5\sigma$).

We compared our results from BASTA with the software ASTROARIADNE[4] (Vines & Jenkins 2022). This python code fits the observed spectral energy distribution via broad-band photometry to atmospheric model grids to obtain the stellar radius. We fitted the bandpasses $GG_{\rm BP}G_{\rm RP}$ (*Gaia* eDR3), *WISE (Wide-field Infrared Survey Explorer) W1 –W2*, JHK_S magnitudes (2MASS, Two Micron All Sky Survey), the Johnson B and V magnitudes (APASS, AAVSO Photometric All-Sky Survey), and the *Gaia* eDR3 parallax. We used the `Phoenix v2` (Husser et al. 2013) and the `BtSettl` (Allard, Homeier & Freytag 2012) atmospheric models. The final radius was computed with Bayesian Model Averaging and the errors with a sampling method for conservative uncertainties as described in Vines & Jenkins (2022). In this way, we obtained a stellar radius of $0.630^{+0.044}_{-0.017}\,R_\odot$. The stellar mass was computed with ARIADNE and the MIST (Choi et al. 2016) isochrones and was found to be $0.651^{+0.015}_{-0.026}$ $M_\odot$. Table 1 gives the stellar parameters derived from our analysis, as well as the comparisons with ARIADNE, which are within 1σ of our results from BASTA.

4 ANALYSIS AND RESULTS

4.1 Transit model

We jointly fit the SPOC Pre-Search Data Conditioning Simple Aperture Photometry light curves from *TESS* Sectors 6 and 32 using the PYMC3 (Salvatier, Wiecki & Fonnesbeck 2016), EXOPLANET[5] (Foreman-Mackey, Barentsen & Barclay 2019), STARRY (Luger et al. 2019), and CELERITE2 (Foreman-Mackey et al. 2017, 2018) software packages.

To account for stellar activity signals and instrumental Systemics we included a Gaussian Process (GP; Rasmussen & Williams 2005) model, using a Matérn-3/2 covariance function. We placed Gaussian priors on the stellar mass and radius based on the results in Table 1. We also placed Gaussian priors on the limb darkening coefficients based on interpolation of the parameters tabulated by Claret, Hauschildt & Witte (2012) and Claret (2017), propagating the uncertainties in the stellar parameters in Table 1 via Monte Carlo simulation.

Visual inspection of the *TESS* light curves reveals quasiperiodic variability with an $\sim$1 ppt amplitude, and their Lomb–Scargle periodograms reveal peaks at $\sim$8 and $\sim$10 d, which are likely the first harmonic of the stellar rotation signal modulo instrumental noise. We thus placed loose Gaussian priors on the GP amplitude and time-scale hyperparameters of 1.0 ± 0.5 ppt and 10 ± 5 d, respectively. The priors used for the transit fit are given in Table A7.

We used separate white noise parameters for each *TESS* sector to account for the possibility of differences in photometric precision, which could potentially arise from different background light conditions or different phases of the spacecraft's operational lifetime. We used the gradient-based `BFGS` algorithm (Nocedal & Wright 2006) implemented in `scipy.optimize` to find initial maximum a posteriori parameter estimates. We used these estimates to initialize an exploration of parameter space via 'no U-turn sampling' (Hoffman & Gelman 2014), an efficient gradient-based Hamiltonian Monte Carlo sampler implemented in PYMC3.

We sampled four chains with 4500 tuning iterations and 3000 additional draws, for a total of 12 000 samples after burn-in; the resulting chains were well-mixed according to a Gelman–Rubin statistic (Gelman & Rubin 1992) value of <1.01, and the sampling error was $\lesssim$1 per cent, suggesting a sufficient number of independent samples had been collected.

The phase-folded *TESS* photometry from Sector 6 and 32, along with the best-fitting transit model, is shown in Fig. 3 and the results of the transit fit are given in Table 2.

4.2 Frequency analysis of HARPS data

We performed a frequency analysis of our RV time-series to search for the Doppler reflex motion induced by the transiting planet discovered by *TESS*, spectroscopically confirm its planetary nature, and possibly unveil the presence of additional signals induced by stellar activity and/or additional orbiting companions. In order

[2] http://www.stsci.edu/~valenti/sme.html
[3] http://vald.astro.uu.se
[4] https://github.com/jvines/astroARIADNE
[5] https://docs.exoplanet.codes/en/stable/

Table 1. Stellar parameters for TOI-544, modelled with SPECMATCH-EMP and SME, and BASTA and ASTROARIADNE . .

Stellar parameters					
Identifiers	TOI-544				
	TIC 50 618 703				
	HD 290498				
Coordinates[a]	05:29:09.62 − 00:20:34.43				
Magnitudes[a]	$V = 10.777 \pm 0.017$				
	$TESS = 9.6504 \pm 0.006$				
Spectroscopic parameters					
Method	$T_{\rm eff}$ (K)	$\log g_\star$ (cgs)	[Fe/H] (dex)	$V \sin i$ (km s^{-1})	Luminosity ($L_\odot$)
SPECMATCH-EMP[b]	4169 ± 70	4.68 ± 0.12	-0.17 ± 0.09	–	–
SME	4248 ± 130	4.60 ± 0.12	-0.15 ± 0.08	2.3 ± 0.8	0.13 ± 0.02
	RA	DEC	Parallax	G	
GAIA[c]	82.2900716	−0.3428983	24.44 ± 0.02	10.41430 ± 0.00059	
Derived parameters					
Method	$M_\star$ ($M_\odot$)	$R_\star$ ($R_\odot$)	Distance (Pc)	Age (Gyr)	
BASTA[d]	0.630 ± 0.018	0.624 ± 0.013	40 ± 1	9 ± 7	
MIST	0.645 ± 0.021	0.617 ± 0.015	40.9 ± 0.03	$5^{+5.3}_{-3.1}$	
ASTROARIADNE	$0.651^{+0.015}_{-0.026}$	$0.630^{+0.044}_{-0.017}$	–	–	

[a]Taken from *TESS* Input Catalogue (TIC) version 8 (Stassun et al. 2019).
[b]Adopted as priors for the stellar mass and radius modelling.
[c]Taken from *Gaia* DR3 (Gaia Collaboration 2021).
[d]Adopted as our final stellar parameter values to be used in analysis of the planetary system.

to avoid having to account for the RV offset between the two spectrographs, we did not include the 14 HARPS-N Doppler data points, and used only the 108 HARPS measurements, which cover a baseline of ∼1051 d (nearly 3 yr), implying a frequency resolution of ∼0.00095 d^{-1}.

Fig. 4 displays the generalized Lomb-Scargle (GLS; Zechmeister & Kürster 2009) periodograms of the HARPS SERVAL RV measurements and of the activity indicators in two frequency ranges. The panels to the left show the periodograms between 0.0 and 0.2 d^{-1}, a range that includes the frequencies at which we expect to detect the Doppler signals induced by active regions corotating with the star. The panels to the right display the periodograms in the range 0.59–0.71 d^{-1}, which encompasses the transit frequency of TOI-544 b. We note that the gap between these frequencies shows nothing of note and is excluded. For each panel, the horizontal dashed line mark the false-alarm probability (FAP) of 0.1 per cent, as derived using the bootstrap method (Murdoch, Hearnshaw & Clark 1993; Kuerster et al. 1997). We considered a peak to be significant if its FAP < 0.1 per cent.

The GLS periodogram of the HARPS RVs (Fig. 4, upper left panel) displays its most significant peak at ∼0.02 d^{-1} (∼50 d). This peak does not appear in any other periodograms of the activity indicators[6], providing evidence that the 50-d signal is very likely caused by an additional companion, which we refer to as TOI-544 c throughout the paper.

We removed the Doppler reflex motion induced by TOI-544 c fixing period and phase to the values derived from the periodogram analysis, while fitting for the RV semi-amplitude and systemic velocity. The periodogram of the RV residuals following the subtraction of the Doppler reflex motion induced by TOI-544 c (Fig. 4, second left panel) shows 3 equally spaced peaks at ∼0.051 d^{-1} (∼19.4 d), ∼0.102 d^{-1} (∼9.8 d), and ∼0.153 d^{-1} (∼6.5 d). The former is significantly detected also in the periodograms of the dLW, CCF-BIS, S-index, Hα, Na D1, and Na D2 lines (Fig. 4, lower left panels), implying that this is very likely due to stellar activity. We interpreted the peak at ∼19.4 d as the stellar rotation period, in excellent agreement with the WASP results (Section 2.2). The two peaks at ∼9.8 and ∼6.5 d are the first and second harmonics of the stellar rotation period, which are likely caused by the presence of spots equally spaced in longitude and/or by the non-coherent nature of the activity-induced signal.

We removed the stellar signal by fitting three Fourier components at the stellar rotation period and its first two harmonics. The GLS periodogram of the RV residuals (Fig. 4, third right panel) shows its strongest power at ∼0.646 d^{-1} (∼1.55 d), the orbital frequency $f_{\rm b}$ of the transiting planet TOI-544 b. Although the FAP of this feature anywhere in the frequency range of the periodogram is higher than 0.1 per cent, the presence of a peak at a known frequency, i.e. the transit frequency, provides strong evidence that this signal is due to planet b. We estimated the FAP at the orbital frequency of TOI-544 b using the windowing bootstrap method described in Hatzes (2019). Briefly, we estimated the bootstrap FAP over a $\Delta\nu = 0.1$ d^{-1} wide frequency window centred on $f_{\rm b}$. We successively narrowed the spectral window at steps of 0.01 d^{-1} for 10 additional bootstrap randomizations, down to $\Delta\nu = 0.01$ d^{-1}. The fit of the FAP versus window size, extrapolated to the intercept (i.e. the zero window length), yields an FAP = 0.004 per cent at $f_{\rm b}$, spectroscopically confirming the planetary nature of the transit signal discovered by *TESS*.

[6]We note that there are two peaks in the periodogram for Hα which are symmetrically located around the peak at ∼0.02 d^{-1}. However, neither these are at the same frequency as the signal, nor they are significant (FAP > 0.1 per cent)

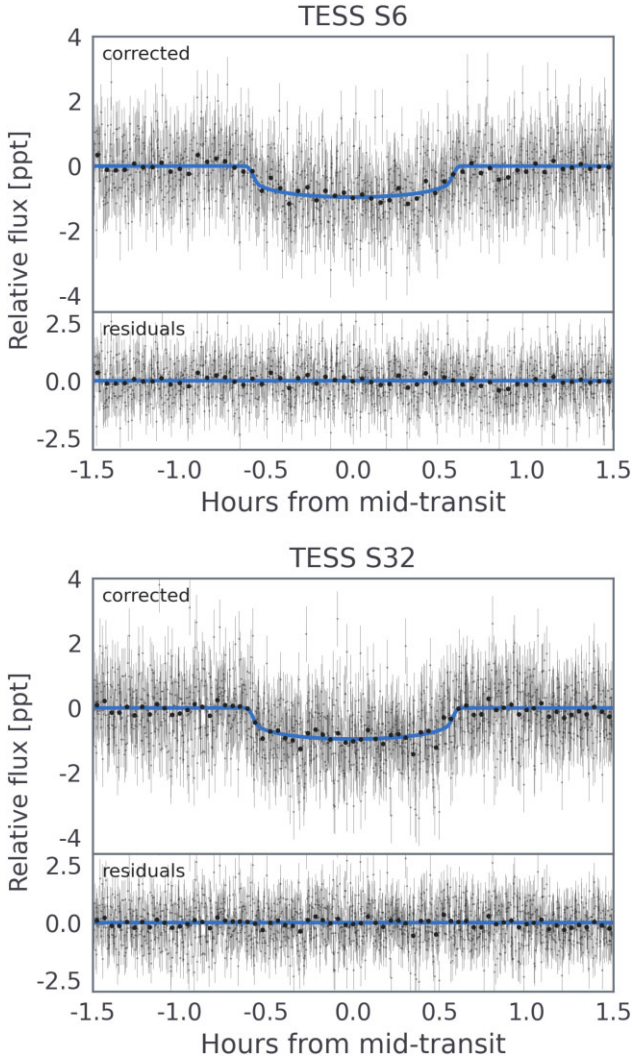

Figure 3. Phase-folded *TESS* photometry from Sector 6 (top) and Sector 32 (bottom), with the best-fitting transit model in blue, the lower panel of each shows the residuals to the best-fitting model. The larger black points show the data binned by a factor of 30.

The periodograms of the FWHM, contrast, dLW, Hα, and Na D1 (Fig. 4, yellow strip) display significant peaks at frequencies $\lesssim 0.01$ d^{-1} ($\gtrsim 100$ d), which are equally spaced by about $1/365 \approx 0.0027$ d^{-1}, i.e. the seasonal sampling of our time series. Hence, most of these peaks are 1-yr aliases of true signals with periods of about 100–250 d. This range includes the evolution time-scale of active regions $\lambda_e = 112^{+28}_{-29}$ d, as inferred by our multi-dimensional Gaussian process analysis (see Section 4.3), suggesting that these signals are associated to long-term stellar variability and spot evolution.

4.3 Radial velocity analysis

We modelled the RV data using the code PYANETI (Barragán, Gandolfi & Antoniciello 2019; Barragán et al. 2022), which implements a multi-dimensional GP to help account for the impact of stellar activity. The implementation of GPs for this purpose is described in detail in Rajpaul et al. (2015). Essentially, this method models the RVs and an activity indicator of choice, assuming that the same GP, $G(t_i, t_j)$, can describe both of them. We used the S-index as the activity indicator to model alongside the RVs. As the RVs and the

Table 2. Results of the transit and RV fit for TOI-544, showing the median value and 68 per cent credible interval for each parameter.

Fitted parameter	Median value
Planet transit parameters	
Stellar mass $M_\star$ ($M_\odot$)	0.631 ± 0.018
Stellar radius $R_\star$ ($R_\odot$)	0.623 ± 0.012
Time of mid-transit T_0 ($BJD_{TDB} - 2450000$)	$9199.031363^{+0.000614}_{-0.000703}$
Orbital period P_b (d)	1.548352 ± 0.000002
$R_b/R_\star$	0.0297 ± 0.0007
Impact parameter b	$0.66^{+0.03}_{-0.04}$
σ_{GP} (ppm)	707^{+113}_{-86}
ρ_{GP} (h)	$22.0^{+3.5}_{-2.8}$
u_1	0.43 ± 0.16
u_2	0.24 ± 0.15
$\log \sigma_{S6}$ (ppt)	$-0.159094^{+0.005981}_{-0.005915}$
$\log \sigma_{S32}$ (ppt)	$-0.157482^{+0.005387}_{-0.005275}$
Planet radius R_b ($R_\oplus$)	2.018 ± 0.076
Semi-major axis a_b (AU)	0.0225 ± 0.0002
Equilibrium temperature T_{eq} (K)	999 ± 14
Transit duration T_{14} (h)	1.21 ± 0.03
Planet RV parameters	
Orbital period, P_b (d)	1.548352 ± 0.000002
Time of inf. conjunction, $T_{conj,b}$ ($BJD_{TDB} - 2450000$)	9199.0314 ± 0.0007
Time of periastron, $T_{peri,b}$ ($BJD_{TDB} - 2450000$)	9198.6443 ± 0.0007
Eccentricity, e_b	$\equiv 0$
Argument of periastron, ω_b (°)	$\equiv 0$
$ew1_b$, $\sqrt{e_b}\sin\omega_b$	$\equiv 0$
$ew2_b$, $\sqrt{e_b}\cos\omega_b$	$\equiv 0$
RV semi-amplitude, K_b (m s^{-1})	2.17 ± 0.36
Planet mass, M_b ($M_\oplus$)	2.89 ± 0.48
Orbital period, P_c (days)	50.089 ± 0.24
Time of inf. conjunction, $T_{conj,c}$ ($BJD_{TDB} - 2450000$)	$9212.0^{+1.8}_{-1.9}$
Time of periastron $T_{peri,c}$ ($BJD_{TDB} - 2450000$)	$9205.4^{+2.2}_{-2.8}$
Eccentricity, e_c	$0.32^{+0.08}_{-0.09}$
Argument of periastron, ω_c (°)	11^{+19}_{-17}
$ew1_c$, $\sqrt{e_c}\sin\omega_c$	0.11 ± 0.17
$ew2_c$, $\sqrt{e_c}\cos\omega_c$	$0.52^{+0.08}_{-0.11}$
RV amplitude, K_c (m s^{-1})	5.36 ± 0.56
Planet minimum mass, $M_c \sin i_c$ ($M_\oplus$)	21.5 ± 2.0
Other parameters	
Offset $RV_{HARPS\text{-}N}$ (km s^{-1})	-0.016 ± 0.002
Offset RV_{HARPS} (km s^{-1})	0.006 ± 0.001
Offset $S\text{-}index_{HARPS\text{-}N}$	1.13 ± 0.03
Offset $S\text{-}index_{HARPS}$	$1.25^{+0.03}_{-0.04}$
Jitter term $RV_{HARPS\text{-}N}$, $\sigma_{HARPS\text{-}N}$ (m s^{-1})	$2.75^{+1.44}_{-1.13}$
Jitter term RV_{HARPS}, σ_{HARPS} (m s^{-1})	$1.85^{+0.36}_{-0.33}$
Jitter term $S\text{-}index_{HARPS\text{-}N}$	$45.5^{+17.7}_{-12.8}$
Jitter term $S\text{-}index_{HARPS}$	$42.6^{+3.5}_{-3.2}$
GP hyperparameters	
A_0	$0.002^{+0.001}_{-0.001}$
A_1	$0.025^{+0.008}_{-0.005}$
A_2	$0.076^{+0.025}_{-0.016}$

Table 2 – *continued*

Fitted parameter	Median value
A_3	$\equiv 0$
λ_e (d)	112^{+28}_{-29}
λ_p	$0.519^{+0.091}_{-0.074}$
Rotation period, P_{GP} (d)	$19.343^{+0.073}_{-0.076}$

S-index of TOI-544 show a significant stellar rotation signal (Fig. 4), we chose the quasi-periodic kernel for the GP

$$G\left(t_i, t_j\right) = \exp\left[\frac{\sin^2\left[\pi\left(t_i - t_j\right)/P_{GP}\right]}{2{\lambda_p}^2} - \frac{\left(t_i - t_j\right)^2}{2{\lambda_e}^2}\right], \quad (1)$$

where P_{GP} is the GP characteristic period (which here represents the stellar rotation period), λ_p is the inverse of the harmonic complexity (related to distribution of active regions on the stellar surface), and λ_e is the long-term evolution time-scale (the lifetime of active regions on the stellar disc). The two-dimensional GP used to model the system is then given by

$$\mathrm{RV} = A_0 G + A_1 \mathrm{d}G \quad (2)$$

and

$$\text{S-index} = A_2 G + A_3 \mathrm{d}G, \quad (3)$$

where A_0, A_1, and A_2 are GP hyperparameters in the form of amplitudes that work as a scale factor that determines the typical deviation from the mean function, and dG is the time derivative of our GP function, $G(t_i, t_j)$. From first principles, $A_3 \equiv 0$, see Rajpaul et al. (2015) for more details. We used the stellar parameters listed in Table 1, and informative Gaussian priors on the orbital period and time of mid-transit for planet b based on those found in the transit fit (Section 4.1). We used the orbital period and time of inferior conjunction we derived from our GLS periodogram to place uniform priors for planet c (see Fig. 4 and Section 4.2 for description of this search). We adopted a uniform prior on P_{GP} centred on the stellar rotation period found by the WASP photometry, and wide uniform priors on the remaining model parameters. PYANETI infers the systemic velocity (aka offset) for each instrument, the exact values found by PYANETI are given in Table 2. We then performed a Markov chain Monte Carlo analysis, fitting for an eccentric orbit for both planets. We sampled the parameter space with 500 Markov chains and used the final set of 5000 steps with a thin factor of 10 to produce our posterior distributions, which led to a total of 250 000 independent points for each sampled parameter.

We find that TOI-544 b has an orbital period of ∼1.55 d and a K_b amplitude (the radial velocity semi-amplitude) of 2.66 ± 0.44 m s^{-1}, equating to a planet mass of 3.28 ± 0.48 M$_\oplus$. The eccentricity of TOI-544 b is found to be $0.35^{+0.14}_{-0.12}$ and its argument of periastron is 41.2^{+17}_{-26} deg. TOI-544 c has a period of 50.1 ± 0.2 d, K_c amplitude of 5.21 ± 0.57 m s^{-1}, implying a minimum mass of 21.0 ± 2.0 M$_\oplus$. The eccentricity of TOI-544 c is found to be 0.30 ± 0.09 and argument of periastron is 17^{+21}_{-18} deg.

We assessed the significance of the eccentric solutions for the two planets by creating 5000 sets of synthetic RV time-series that sample the best-fitting circular solutions at the epochs of our real observations. We added Gaussian noise at the same level of our RV measurement uncertainties and fitted the simulated time series allowing for non-zero eccentricities. For TOI-544 b, there is an ∼3.5 per cent that a best-fitting eccentric solution with $e \geq 0.35$ could arise by chance if the orbit is actually circular. As for TOI-544 c, the probability that noise can account for $e \geq 0.30$ is only 0.2 per cent. Assuming a significance level of 1 per cent, the eccentric solution for TOI-544 b is likely not real, while the eccentricity of TOI-544 c is real. Therefore, our adopted results are for the case where the inner planet is on a circular orbit and outer planet is on an eccentric orbit, i.e. TOI-544 b has an orbital period of ∼1.55 d and a K_b amplitude of 2.17 ± 0.36 m s^{-1}, equating to a planet mass of $M_b = 2.89 \pm 0.48$ M$_\oplus$, TOI-544 c has a period of 50.1 ± 0.2 d, K_c amplitude of 5.36 ± 0.55 m s^{-1}, implying a minimum mass of $M_c \sin i_c = 21.5 \pm 2.0$ M$_\oplus$. The eccentricity of TOI-544 c is found to be $e_c = 0.32 \pm 0.09$ and argument of periastron is $\omega_c = 12^{+19}_{-17}$ deg.

The priors used for all parameters are shown in Table A6, and the results, showing the median value and 68 per cent credible interval for each parameter, are given in Table 2. The best-fitting model alongside the data are shown, as a function of time, in Fig. 5 and phase-folded for each planet in Fig. 6.

We additionally chose to model the RV data using several other methods to ensure the robustness of our results. Using PYANETI, we ran similar fits to the one described above, but with: (a) both planets on circular orbits; (b) the inner planet on a circular orbit and the outer planet on an eccentric orbit; (c) a fit with PYANETI but not multi-dimensional (i.e. fitting on only the RV data points); (d) a joint model including both transit and RV data. Our joint fit of transit and RV data provides consistent results with the planet mass within 1σ of our other models (see Table A5).

We also make use of the radial velocity fitting toolkit `RadVel` (Fulton et al. 2018). Using `RadVel` we ran fits for: (a) a two planet system with no GP to account for stellar activity; (b) a one planet system (only the transiting inner planet) including a GP using the Celerite quasi-periodic kernel (Foreman-Mackey et al. 2017); (c) a two planet system using the Celerite quasi-periodic kernel where both planets are on circular orbits; (d) the same kernel again but where both planets are on eccentric orbits; (e) a two planet system where we use the square-exponential GP kernel (described in Fulton et al. 2018). As well as this, we checked for possible additional signals by fitting for a three-planet system. We found that the third signal is unconstrained and the Bayesian information criterion (BIC) and Akaike information criterion (AIC) increase slightly over the two-planet case – therefore we do not believe there are signs of additional planets in the system. We also changed the choice of priors in our models, in particular for the period of planet c to ensure we are not biasing our results. For example, the `RadVel` fit for a two-planet system with the square exponential kernel has a uniform prior on P_c of 0 to 100 d, and the `RadVel` fit for a two-planet system with the Celerite quasi-periodic kernel has a Gaussian prior of 50.6 ± 1.0 d. In all cases the results are consistent. The resulting K semi-amplitude and mass of TOI-544 b found from all models are shown in Table A5.

`RadVel` also allows for model comparison. We found that in models which include more than one planet, a single-planet model is ruled out in every case – providing greater assurance of the existence of the second planet. Specifically, for a one-planet system, the BIC is 1993.90 and AIC is 1965.46, and for two-planet system 801.24 and 765.90, respectively. We also ran additional models using only the HARPS data points to ensure the HARPS-N points (which have a slightly higher level of scatter) are not influencing our fit, and with RVs extracted with TERRA rather than SERVAL, in all cases the results are consistent within 1σ. As well as this, we ran PYANETI fits with different activity indicators: FWHM, and contrast, and combinations of indicators: *S*-index and FWHM, *S*-index and contrast, and FWHM and contrast. In all cases the derived planet parameters are consistent with our other models within 1σ, however the GP hyperparameters

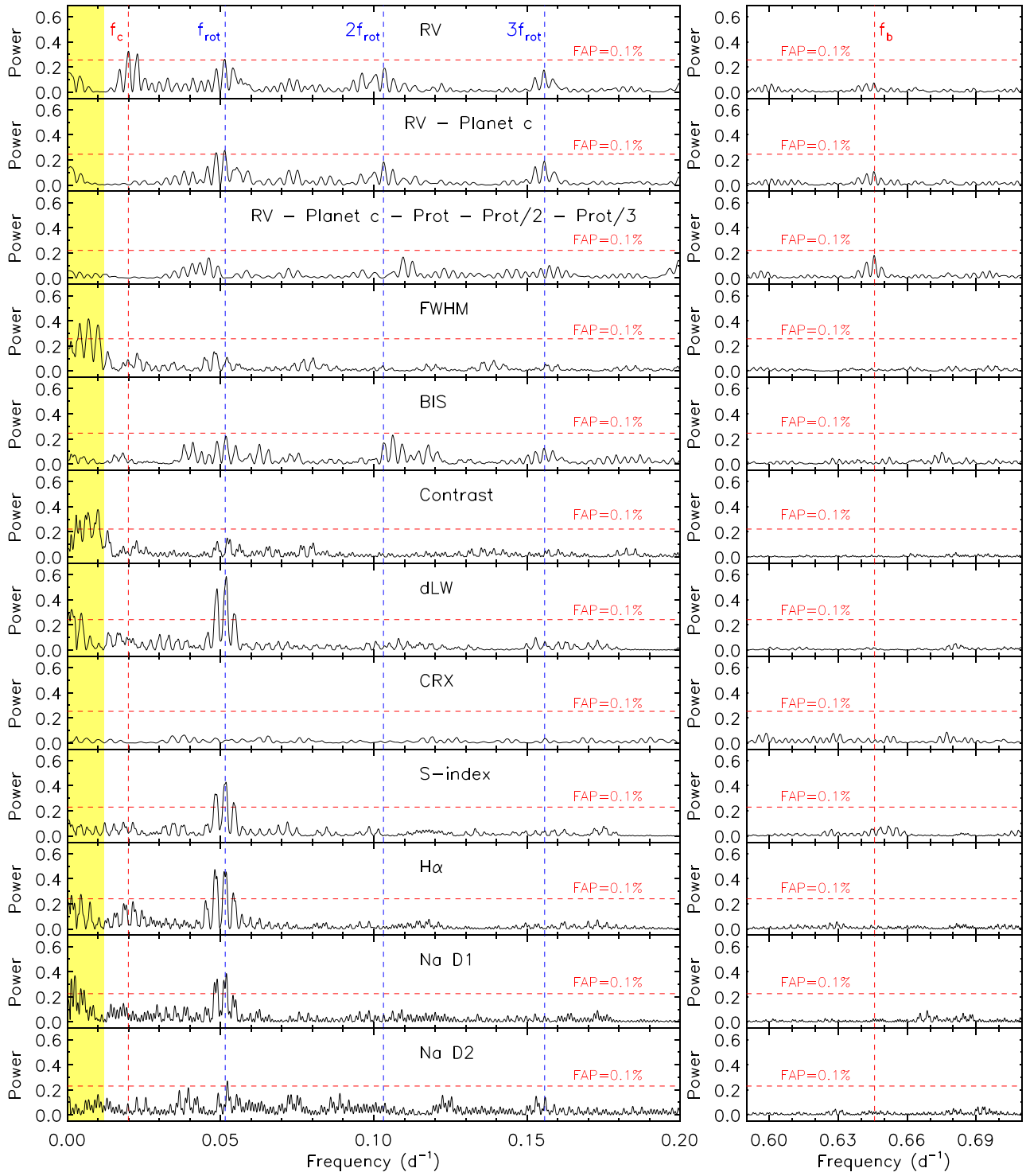

Figure 4. Generalized Lomb–Scargle periodograms of the SERVAL RV measurements and activity indicators of TOI-544. The right and left columns cover two frequency ranges encompassing the orbital frequency of TOI-544 c, the stellar rotation frequency and its first two harmonics (left panels), and the orbital frequency of TOI-544 b (right panels). The Doppler signals from the two planets are marked as vertical red dashed lines at $f_c \approx 0.02\,d^{-1}$ (TOI-544 c) and $f_b \approx 0.646\,d^{-1}$ (TOI-544 b). Vertical, blue dashed lines indicate the stellar rotation frequency ($f_{rot} \approx 0.051\,d^{-1}$) and its first two harmonics ($2f_{rot} \approx 0.102\,d^{-1}$ and $3f_{rot} \approx 0.153\,d^{-1}$). The horizontal red dashed line mark the 0.1 per cent false alarm probability. The shaded yellow band highlights the frequency range encompassing the long-period activity signals that we significantly detected in the the FWHM, contrast, dLW, Hα, and Na D1, and that are likely related to spot evolution, along with their 1-yr aliases (Section 4.2), last paragraph. *From top to bottom:* the SERVAL RV measurements; RV residuals following the subtraction of the Doppler reflex motion induced by TOI-544 c; RV residuals after subtracting the signals of the star rotation, its first two harmonics, and TOI-544 c; FWHM; BIS; contrast; dLW; CRX; S-index; Hα; Na D1; Na D2.

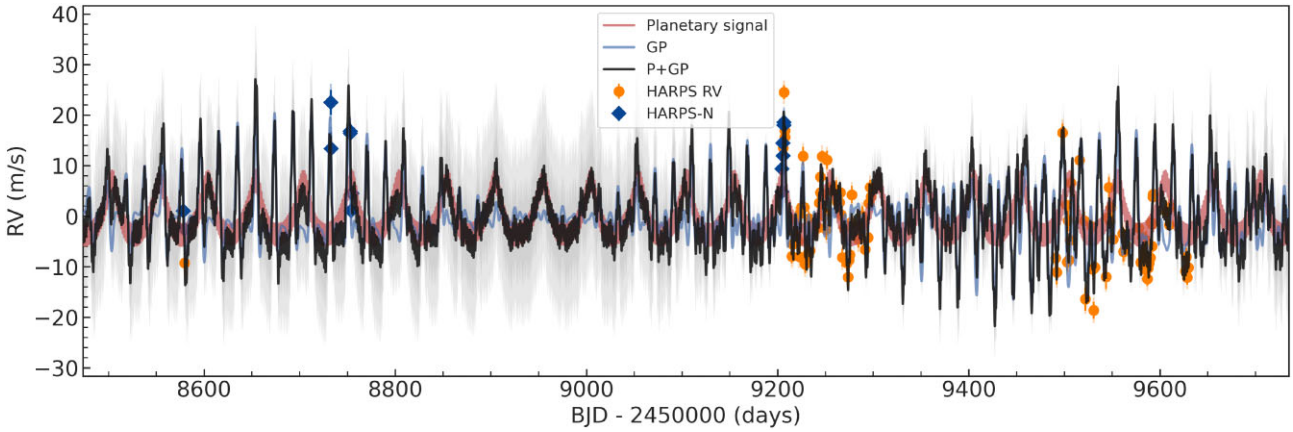

Figure 5. Best-fitting 2-planet Keplerian orbital model for TOI-544. HARPS data shown by orange circles, and HARPS-N data shown by blue diamonds, both shown as a function of time. The best-fitting model for the planet signals is shown in red, the GP model in blue, and the combined planets and GP shown in black. The dark and light shaded areas showing the 1σ and 2σ credible intervals of the corresponding GP model, respectively.

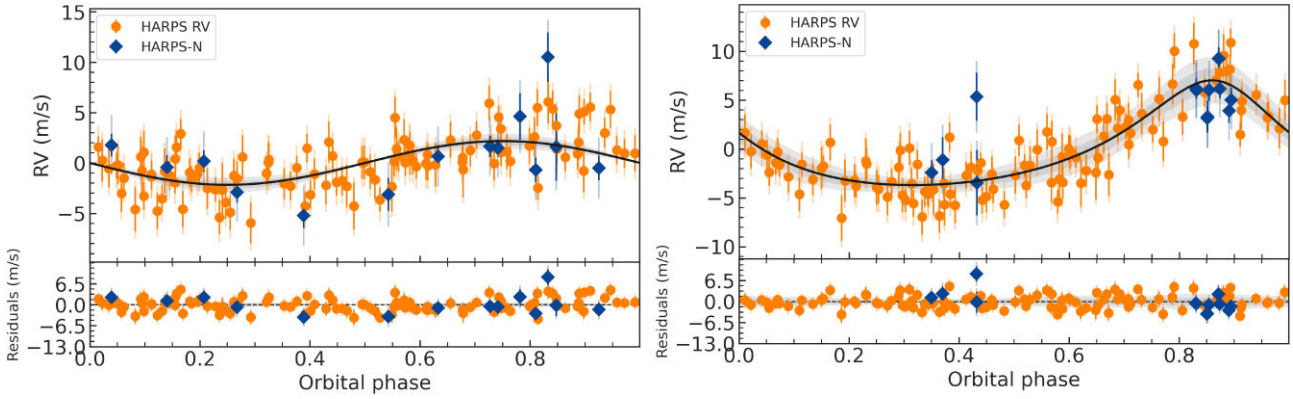

Figure 6. The phase-folded RV data from HARPS (orange circles) and HARPS-N (blue diamonds) alongside the best-fitting planet model (with the effect of the other planet and the GP model subtracted from each). TOI-544 b is on the left and TOI-544 c on the right. The lower part shows the residuals from the fit. There appears to be no trends visible in the residuals, and the augmented sinusoid representative of an eccentric orbit is present in both phase-folded plots.

are not all so well constrained so we still use the model with the *S*-index as our adopted results.

5 DISCUSSION

5.1 Composition of TOI-544 b

The calculated density of TOI-544 b is $\rho_b = 1.93^{+0.30}_{-0.25}$ g cm^{-3}, which is not dense enough to be composed of entirely rock and iron, where densities are typically between 3 and 10 g cm^{-3} (Zeng et al. 2019). This implies that a composition of a bare rocky-iron core can likely be excluded. TOI-544 b must have some additional component to its composition, but whether it is in the form of water/ice layers or a H–He atmosphere depends on which particular composition models are used. Fig. 7, left panel, shows the mass–radius diagram for small planets (< 4 R$_\oplus$, with mass uncertainties <20 per cent) with TOI-544 b highlighted and composition tracks from Zeng et al. (2019) shown in different colours. As noted in Rogers, Schlichting & Owen (2023), these models are often misinterpreted when used in mass–radius diagrams. Specifically, there are a range of models available depending on the chosen temperature, this temperature is often assumed to be the equilibrium temperature of the planets but is actually the temperature at a pressure of 100 bars. In this case, we have used the *incorrect* temperature (equal to the planet equilibrium temperature of $\approx$1000 K) in order to show a direct comparison to many other mass–radius diagrams available in the literature. Using these models alone, it appears that TOI-544 b does not fit the super-Earth (rocky/iron core) scenario, and that it also does not fit the typical sub-Neptune composition of a rocky core surrounded by atmospheric H–He. From these models it seems likely that TOI-544 b is a water-world planet with a sizeable fraction of H_2O present. From the Zeng et al. (2019) models it seems that a water fraction by mass of over 50 per cent is possible for this planet. There are few other planets detected in a similar area of parameter space, however we note that many of the planets in this regime have multiple mass values listed on the NASA Exoplanet Archive so their exact location on the mass–radius diagram depends on the specific choice of literature parameters, and many have longer orbital periods, meaning it is difficult to do a real comparison.

To further investigate the compositional nature of the planet, we use the dimensionless parameter ζ from Zeng et al. (2021)

$$\zeta \equiv \frac{(R_c/R_\oplus)}{(M_c/M_\oplus)^{0.25}}, \tag{4}$$

where R_C and M_C are the core radius and mass, respectively, similar to the approach taken in Nava et al. (2019). This parameter can be used to distinguish between the three possible compositions of small

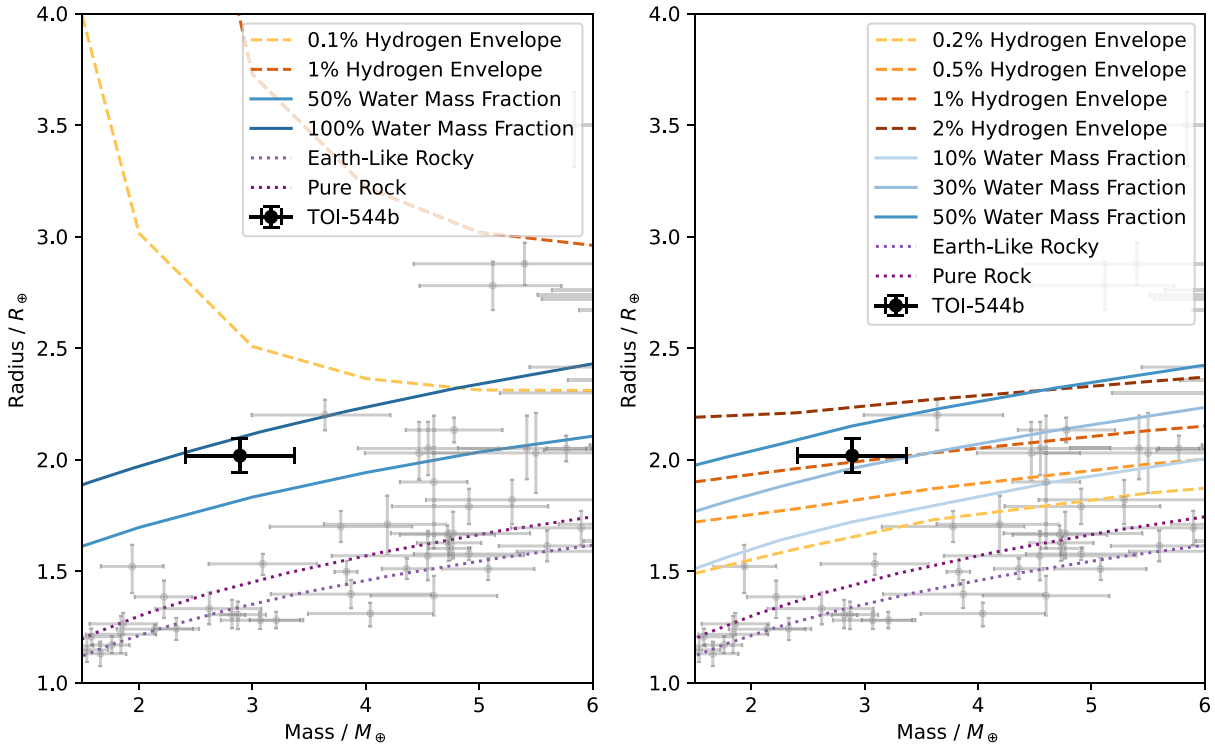

Figure 7. Mass–radius diagram showing confirmed planets with mass uncertainties <20 per cent in grey circles, with TOI-544 b shown as the black circle. Left: the coloured tracks show different potential planet compositions from Zeng et al. (2019), assuming a planetary equilibrium temperature of 1000 K. The dashed lines show compositions of an Earth-like rocky core surrounded by a layer of H–He in varying percentages by mass, the solid lines show water world compositions with varying water mass fractions, the dotted lines show rocky and Earth-like rocky compositions. TOI-544 b is closest to the tracks with 100 per cent H_2O and 50 per cent H_2O with 50 per cent rock. Right: the same as the left panel but the the dashed lines show compositions of an Earth-like rocky core surrounded by a layer of H–He in varying percentages by mass from Lopez & Fortney (2014) using the models for a 10 Gyr planet, with solar metalicity and flux of 10 $F_\oplus$, the solid lines show compositions from Aguichine et al. (2021) of irradiated ocean worlds with varying water mass fractions, and the dotted lines show the same rocky and Earth-like rocky compositions from Zeng et al. (2019). TOI-544 b is closest to models with either 30 per cent water mass fraction, or a rocky core with a Hydrogen envelope of between 0.5 and 1 per cent. The data is downloaded from the NASA Exoplanet Archive.

exoplanets – either rocky and earth-like ($\zeta = 1$), having significant amounts of ices ($\zeta = 1.4$), or icey cores with hydrogen/helium envelopes ($\zeta = 2.2$). For small planets the core radius and mass can be approximated the planet radius and mass (in units of Earth radii and mass). The value of ζ for TOI-544 b is 1.5, which suggests an ice dominated composition.

Another approach is noting that TOI-544 b is a highly irradiated planet due to its short semi-major axis. We make use of the `Structure Model INterpolator (SMINT)`[7] which obtains posterior distributions of H_2O mass fraction based on interpolation on to the Aguichine et al. (2021) model grids. Using the stellar and planetary parameters listed previously, with conservative uncertainties, we obtain an H_2O fraction of 0.25 ± 0.12. This is lower than the expected H_2O fraction seen in the mass–radius diagram. We note, however, that the models from Zeng et al. (2019) do not account for the high level of radiation such a close-in planet would receive.

However, whilst Zeng et al. (2019) models are commonly used in mass–radius diagrams for small planets, Rogers, Schlichting & Owen (2023) recommend using the mass–radius relations for sub-Neptune compositions given in Lopez & Fortney (2014), which assume a constant planet age, rather than the Zeng et al. (2019) models which assume a constant specific entropy. In the right panel of Fig. 7, we plot a mass–radius diagram with composition tracks from Lopez & Fortney (2014) and Aguichine et al. (2021). The dashed lines show compositions of an Earth-like rocky core surrounded by a layer of H–He in varying percentages by mass from Lopez & Fortney (2014). The solid lines show compositions from Aguichine et al. (2021) of irradiated ocean worlds with varying water mass fractions. The dotted lines show the same rocky and Earth-like rocky compositions from Zeng et al. (2019) which are shown in the left panel. Setting TOI-544 b on this graph, we see that according to the Lopez & Fortney (2014) models, a composition of an Earth-like core surrounded by a layer of H–He of between 0.5 and 1 per cent by mass can also explain the observed mass and radius. The composition tracks from Aguichine et al. (2021) for irradiated water-worlds suggest an alternative composition of TOI-544 b of a rocky core with a layer of water/ice of around 30 per cent by mass.

As discussed in Rogers, Schlichting & Owen (2023), for individual planets such as TOI-544 b, mass and radius alone are insufficient to uniquely constrain planet composition. In order to break the degeneracy between the water-worlds and sub-Neptune models, atmospheric observations of the planet are needed to rule out (or in) the potential for H–He or H_2O atmospheres. Fortunately, as described in Section 5.4, TOI-544 b is an ideal candidate for atmospheric studies. Future observations, with for instance *JWST*, should be able to help determine more definitively whether this is a water-world or not.

[7] https://github.com/cpiaulet/smint

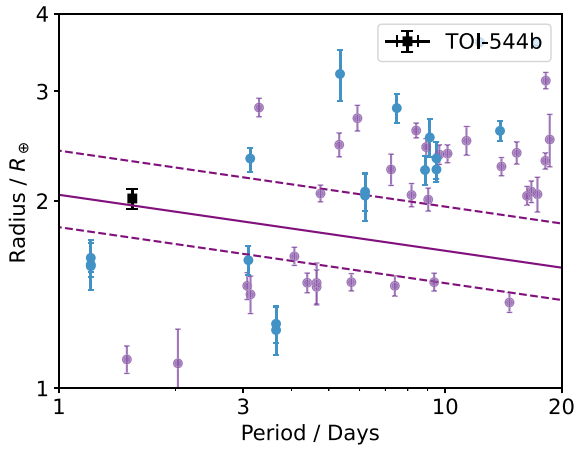

Figure 8. Period–radius diagram for a subset of confirmed planets orbiting stars with masses <0.8 $M_\odot$. Purple circles are confirmed Kepler planets fitted in a homogeneous way in Ho & Van Eylen (2023). Blue circles show planets with precise mass measurements from the NASA Exoplanet Archive. TOI-544 b shown by the black square. TOI-544 b sits within the expected location of the radius valley (between the dashed lines) for this specific stellar mass – calculated from equation 11 in Ho & Van Eylen (2023).

From Fig. 7, it can also be seen that TOI-544 b sits within an area of the mass–radius diagram where few planets have been observed. Of the more than 5000 exoplanets confirmed to date, there are less than 200 small (<4 $R_\oplus$) planets which have precisely characterized masses (uncertainties <20 per cent), and of those, less than 30 are low mass (<4 $M_\oplus$). The majority of these small, low mass planets with precise characterization cluster around the composition tracks for rocky silicates or iron composition – similar to an Earth-like composition. The most similar planet is Kepler-307c, which is one of the only low-mass planets that has a similarly low density (seen to the top right of TOI-544 b in Fig. 7). The mass of Kepler-307c was determined through transit timing variations rather than through RV observations. As there have been suggestions of a potential offset between the two methods (Steffen 2016; Mills & Mazeh 2017), it is possible that these two planets are not fully comparable. In general, there are few precisely characterized masses for small planets, and even fewer for potential water-worlds, meaning TOI-544 b is an important addition to this region of parameter space.

5.2 Location in relation to the radius valley

In the most recent comprehensive study of the radius valley, Ho & Van Eylen (2023) refitted Kepler data to find an empirical radius valley location, as a function of various other parameters. In particular, they find a dependence on the location of the valley as a function of stellar mass. Fig. 8 shows the period–radius diagram for confirmed Kepler planets orbiting stars with stellar mass <0.8 $M_\odot$ fitted in a homogeneous way in Ho & Van Eylen (2023). Additionally, planets with precise mass measurements from the NASA Exoplanet Archive which orbit stars with masses <0.8 $M_\odot$ are highlighted, and TOI-544 b shown. TOI-544 b sits within the radius valley region calculated for this specific stellar mass – using equation 11 from (Ho & Van Eylen 2023):

$$\log_{10}(R_\mathrm{p}/R_\oplus) = A\ \log_{10}(P/\mathrm{d}) + B\ \log_{10}(M_*/M_\odot) + C \qquad (5)$$

with $A = -0.09^{+0.02}_{-0.03}$, $B = 0.21^{+0.06}_{-0.07}$, $C = 0.35^{+0.02}_{-0.02}$ and using TOI-544's stellar mass (see Table 1). TOI-544 b is more than 3σ away from the upper and lower bounds of the radius valley (shown by the dashed lines). We also ran a number of fits for stellar radius; we use the calculated stellar radii from 1, taking the most extreme cases of the BASTA fit -1σ, and the ASTROARIADNE fit $+1\sigma$ (i.e.the smallest and largest possible from our results), we find planet radii of 2.16 and 1.98 $R_\oplus$, respectively. These values still put TOI-544 within the limits of the valley given in Ho & Van Eylen (2023).

We also compare the location of the radius valley presented in Ho & Van Eylen (2023) with other works. In particular, Petigura et al. (2022) also find that the location of the valley varies based on stellar mass, finding a similar relation to equation (5). For a star of mass 0.5–0.7 $M_\odot$, Fig. 8 in Petigura et al. (2022) shows that TOI-544 b would be inside the valley. Cloutier & Menou (2020) also investigated the location of the radius valley for low-mass (mid-K to mid-M dwarf) stars and similarly find that a planet such as TOI-544 b, with radius of $2.018 \pm 0.076\,R_\oplus$ and orbital period of 1.55 d would be located inside the valley in the region they dub 'keystone planets', see fig. 15 of Cloutier & Menou (2020).

The observational results for the location of the radius valley can be compared with theoretical models such as in Owen & Wu (2017), which predicts that the location of the valley also depends on the planetary core composition. If we assume that planets form uniformly with an icey core – rather than a rocky one – then the theoretical models predict that the radius valley will be shifted to a higher radius for a given orbital period. This means that, for planets with icey cores – sometimes referred to as water world planets – the location of TOI-544 b in the radius-period space would not put it inside the radius valley. Instead it would sit below the valley, in a region which predicts planets with a sizeable water/ice faction but without significant hydrogen/helium atmospheres, potentially having undergone atmospheric loss.

Luque & Pallé (2022) argue that the radius valley distribution may in fact be the result of two different core compositions of planets rather than purely from atmospheric loss mechanisms, in the case of planets orbiting M-dwarfs. They state that small planets come in two distinct types: super-Earths with rocky/iron composition, and water worlds with a combination of both rock and water/ices. This interpretation is disputed by Rogers, Schlichting & Owen (2023), who argue that the properties of the sample of planets around M-dwarfs studied by Luque & Pallé (2022) can also be explained by the more traditional super-Earth sub-Neptune classifications which arise from atmospheric loss models.

We note that at this stage there is no conclusive evidence either way to support the water worlds versus atmospheric loss explanation of the radius valley, and further investigation is needed to fully distinguish between the two theories. In particular, confirmation of TOI-544 b as a water world or not (as well as other small planets) would help to provide evidence for the formation mechanisms which carve the radius valley.

5.3 Planet c

We searched the *TESS* light curves for signs of a transit of TOI-544 c but none were found. If we assume that both planets are at the same orbital inclination (which may not be the case) then planet c would not be expected to transit given its impact parameter of 5. As a result, we can only constrain a minimum mass for TOI-544 c of $21.5 \pm 2.0\,M_\oplus$, for reference this is slightly higher than the mass of Neptune. Planet c is found to have a non-zero eccentricity, and, if it is confirmed that TOI-544 b has a large fraction of water within its composition, then it is likely that it must have formed exterior to the snow-line, and then migrated inwards – this migration could have been facilitated by TOI-544 c. A full dynamical investigation of the

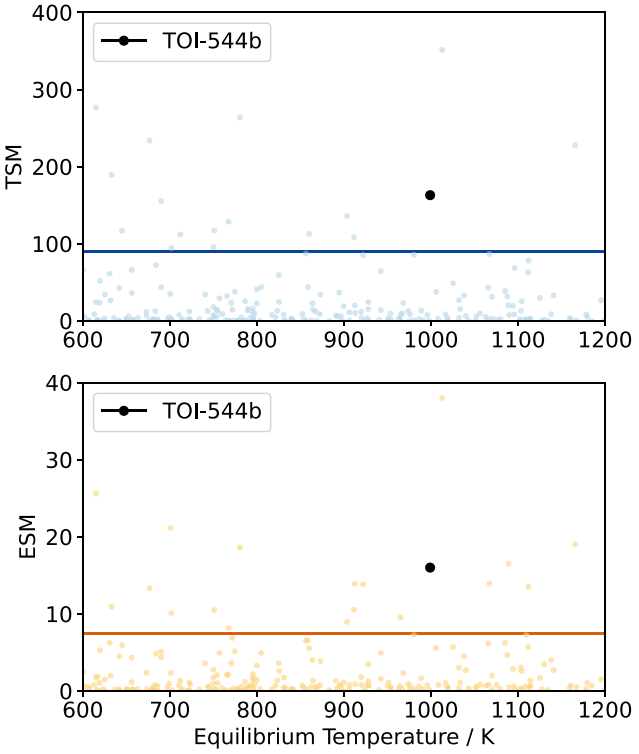

Figure 9. Top panel: The TSM against equilibrium temperature of all small ($R < 4\,R_\oplus$) confirmed planets with a mass measurement, blue dots. The threshold given in Kempton et al. (2018) is shown by the solid line. TOI-544 b is shown in the black circle, it is within the top 15 planets for TSM value. Bottom Panel: Same as above but for the ESM. TOI-544 b is within the top 10 planets for ESM value. The data is downloaded from the NASA Exoplanet Archive.

system architecture is beyond the scope of this paper, but could be interesting in the future, particularly if the composition of the inner planet is better constrained, and it is possible that if the planets do not orbit in the same plane then plant c could in fact transit.

5.4 Potential atmospheric studies of TOI-544 b

We calculated the transmission spectroscopy metric (TSM; Kempton et al. 2018) for TOI-544 b, finding a value of 163, much higher than the recommended threshold value (90) from (Kempton et al. 2018) for planets with radii above 1.5 $R_\oplus$, placing TOI-544 b among the most appealing targets for transmission spectroscopy characterization with *JWST* (within the top 15 targets for similar planets, see Fig. 9). Moreover, the emission spectroscopic metric (ESM; Kempton et al. 2018) is found to be 16. Considering the Kempton et al. (2018) cutoff of 7.5, TOI-544 b lies among the top 10 most favourable targets (see Fig. 9). TOI-544 b is within the top 5 targets for both TSM and ESM for planets with radii between 1.5 and 2.75 $R_\oplus$ and temperature between 800 and 1250 K, as identified by the *TESS* follow-up atmospheric working group. We also calculate the predicted S/N ratio for atmospheric observations of TOI-544 b with *JWST* (using the method in Niraula et al. (2017), finding a value of 1.000. This puts TOI-544 b within the top dozen small planets with temperature less than 1250 K in terms of potential *JWST* observations. Atmospheric observations should help to reduce the degeneracy between composition models for this planet and determine whether a water world or a rocky and hydrogen composition is more likely, similar to a recent study of TOI-270 d (Van Eylen et al. 2021) for which transmission spectroscopy revealed a possible hydrogen-rich atmosphere (Mikal-Evans et al. 2022).

6 CONCLUSIONS

We present the results of an extensive high-precision RV campaign of TOI-544. We confirm the planet TOI-544 b and derive a mass of $M_b = 2.89 \pm 0.48\,M_\oplus$ which, combined with the planetary radius of $R_b = 2.018 \pm 0.076\,R_\oplus$ gives a bulk density of $\rho_b = 1.93^{+0.30}_{-0.25}$ g cm^{-3}. The density of the planet means it most likely has either a significant fraction of ice within its composition (around 30 per cent by mass) or is composed of an Earth-like rocky core surrounded by a layer of atmospheric H–He (around 0.5–1 per cent by mass). TOI-544 b also sits within the expected location of the small planet radius valley for FGK stars, although improvements in the radius measurement with additional transit observations would help confirm this further. The calculated TSM and ESM of TOI-544 b put it within the top few planets for atmospheric observations with similar size and temperature, meaning it is an excellent candidate for future observations with *JWST*. We additionally confirm the existence of a second, non-transiting planet within the system, TOI-544 c, with a minimum mass of $M_c \sin i_c = 21.5 \pm 2.0\,M_\oplus$. Both planets have well-characterized masses (uncertainties of <20 per cent) and contribute to the small but growing number of small planets with precisely characterized masses.

ACKNOWLEDGEMENTS

We thank the anonymous reviewer for reviewing the paper, and for their valuable suggestions which have improved the manuscript. This work is done under the framework of the KESPRINT collaboration (http://kesprint.science). KESPRINT is an international consortium devoted to the characterization and research of exoplanets discovered with space-based missions. Based on observations made (a) with ESO-3.6m telescope at La Silla Observatory (Chile) under programme IDs 106.21TJ.001, 0103.C-0442, and 60.A-9709; (b) with the Italian Telescopio Nazionale Galileo (TNG) operated on the island of La Palma in the Spanish Observatorio del Roque de los Muchachos (ORM) by the INAF-Fundación Galileo Galilei, under programme IDs CAT19A_162 and CAT19A_97. We are extremely grateful to the ESO and TNG staff members for their unique and superb support during the observations. This research has made use of the NASA Exoplanet Archive, which is operated by the California Institute of Technology, under contract with the National Aeronautics and Space Administration under the Exoplanet Exploration Program. We are grateful to Cynthia Ho for discussions on the small planet radius valley and James Owen for discussion on use of planet composition tracks. HLMO would also like to thank the Science and Technology Facilities Council (STFC) for funding support through a PhD studentship. CMP gratefully acknowledge the support of the Swedish National Space Agency (DNR 65/19). GN thanks for the research funding from the Ministry of Education and Science programme the 'Excellence Initiative – Research University' conducted at the Centre of Excellence in Astrophysics and Astrochemistry of the Nicolaus Copernicus University in Toruń, Poland. RL acknowledges funding from University of La Laguna through the Margarita Salas Fellowship from the Spanish Ministry of Universities ref. UNI/551/2021-May 26, and under the EU Next Generation funds. APH and ME acknowledge the support of DFG Grant HA 3279/12-1 within the DFG Schwerpunkt SPP 1992, Exploring the Diversity of Extrasolar Planets. HJD acknowledges support from the Spanish Research Agency of the Ministry of Science and

Innovation (AEI-MICINN) under grant PID2019-107061GB-C66, DOI: 10.13039/501100011033. KWFL was supported by Deutsche Forschungsgemeinschaft grants RA714/14-1 within the DFG Schwerpunkt SPP 1992, Exploring the Diversity of Extrasolar Planets. JSJ greatfully acknowledges support by FONDECYT grant 1201371 and from the ANID BASAL project FB210003. JK gratefully acknowledges the support of the Swedish National Space Agency (SNSA; DNR 2020–00104) and of the Swedish Research Council (VR: Etableringsbidrag 2017–04945).

DATA AVAILABILITY

This paper includes raw data collected by the *TESS* mission, which are publicly available from the Mikulski Archive for Space Telescopes (MAST, https://archive.stsci.edu/tess). Some of the observations made with HARPS at the ESO 3.6m telescope (programme 0103.C-0442(A)) are publicly available at the ESO archive (http://archive.eso.org/), observations which are not currently available will become open access within the next year. All processed data underlying this article (including observations from HARPS-N) are available in the article.

REFERENCES

Aguichine A., Mousis O., Deleuil M., Marcq E., 2021, ApJ, 914, 84
Aguirre Børsen-Koch V. et al., 2022, MNRAS, 509, 4344
Allard F., Homeier D., Freytag B., 2012, Phil. Trans. R. Soc., 370, 2765
Anglada-Escudé G., Butler R. P., 2012, ApJS, 200, 15
Baranne A. et al., 1996, A&AS, 119, 373
Barragán O., Gandolfi D., Antoniciello G., 2019, MNRAS, 482, 1017
Barragán O., Aigrain S., Rajpaul V. M., Zicher N., 2022, MNRAS, 509, 866
Cadieux C. et al., 2022, AJ, 164, 96
Choi J., Dotter A., Conroy C., Cantiello M., Paxton B., Johnson B. D., 2016, ApJ, 823, 102
Claret A., 2017, A&A, 600, A30
Claret A., Hauschildt P. H., Witte S., 2012, A&A, 546, A14, New limb-darkening coefficients for PHOENIX/1D model atmospheres. I. Calculations for 1500 K < T_{eff} < 4800 K Kepler, CoRot, Spitzer, uvby, UBVRIJHK, Sloan, and 2MASS photometric systems
Cloutier R., Menou K., 2020, AJ, 159, 211
Collier Cameron A., Jardine M., 2018, MNRAS, 476, 2542
Cosentino R. et al., 2012, in Proc. SPIE Conf. Ser. Vol. 8446, Ground-based and Airborne Instrumentation for Astronomy IV. SPIE, Bellingham, p. 84461V
Diamond-Lowe H. et al., 2022, AJ, 164, 172
Estrela R., Swain M., Gupta A., Sotin C., Valio A., 2020, AJ, 898, 104
Foreman-Mackey D., 2018, Res. Notes Am. Astron. Soc., 2, 31
Foreman-Mackey D., Agol E., Ambikasaran S., Angus R., 2017a, AJ, 154, 220
Foreman-Mackey D., Barentsen G., Barclay T., 2019, dfm/exoplanet: exoplanet v0.1.5
Fridlund M. et al., 2017, A&A, 604, A16
Fulton B. J. et al., 2017, AJ, 154, 109
Fulton B. J., Petigura E. A., Blunt S., Sinukoff E., 2018, PASP, 130, 044504
Gaia Collaboration, 2021, A&A, 649, A1
Gelman A., Rubin D. B., 1992, Stat. Sci., 7, 457
Giacalone S. et al., 2022, AJ, 163, 99
Goffo E. et al., 2023, ApJ, 955, L3
Gray D. F., 2008, The Observation and Analysis of Stellar Photospheres. Cambridge Univ. Press, Cambridge
Green G. M., Schlafly E., Zucker C., Speagle J. S., Finkbeiner D., 2019, ApJ, 887, 93
Gupta A., Schlichting H. E., 2019, MNRAS, 487, 24
Gupta A., Schlichting H. E., 2021, MNRAS, 504, 4634
Gupta A., Nicholson L., Schlichting H. E., 2022, MNRAS, 516, 4585
Hatzes A. P., 2019, The Doppler Method for the Detection of Exoplanets. IoP Publishing, Bristol (Institute of Physics)
Hidalgo S. L. et al., 2018, ApJ, 856, 125
Ho C. S. K., Van Eylen V., 2023, MNRAS, 519, 4056
Hoffman M. D., Gelman A., 2014, J. Mach. Learn. Res., 15, 1593
Husser T. O., Wende-von Berg S., Dreizler S., Homeier D., Reiners A., Barman T., Hauschildt P. H., 2013, A&A, 553, A6
Jenkins J. M. et al., 2016, Proc. SPIE Conf. Ser. Vol. 9913, Software and Cyberinfrastructure for Astronomy IV. SPIE, Bellingham, p. 99133E
Kempton E. M. R. et al., 2018, PASP, 130, 114401
Kuerster M., Schmitt J. H. M. M., Cutispoto G., Dennerl K., 1997, A&A, 320, 831
Kurucz R. L., 2013, Astrophysics Source Code Library, preprint ascl:1303.024
Lopez E. D., Fortney J. J., 2014, ApJ, 792, 1
Lopez E. D., Rice K., 2018, MNRAS, 479, 5303
Lovis C., Pepe F., 2007, A&A, 468, 1115
Luger R., Agol E., Foreman-Mackey D., Fleming D. P., Lustig-Yaeger J., Deitrick R., 2019, AJ, 157, 64
Luque R., Pallé E., 2022, Science, 377, 1211
Luque R. et al., 2021, A&A, 645, A41
Maxted P. F. L. et al., 2011a, PASP, 123, 547
Maxted P. F. L. et al., 2011b, MNRAS, 418, 1156
Mikal-Evans T. et al., 2022, AJ, 165, 84
Mills S. M., Mazeh T., 2017, ApJ, 839, L8
Morton T. D., 2015, Astrophysics Source Code Library, record ascl:1503.010
Murdoch K. A., Hearnshaw J. B., Clark M., 1993, ApJ, 413, 349
Nava C., López-Morales M., Haywood R. D., Giles H. A. C., 2019, AJ, 159, 23
Niraula P. et al., 2017, AJ, 154, 266
Nocedal J., Wright S. J., 2006, Numerical Optimization, 2nd edn. Springer, New York, NY, USA
Owen J. E., Wu Y., 2017, AJ, 847, 29
Pepe F., Mayor M., Galland F., Naef D., Queloz D., Santos N. C., Udry S., Burnet M., 2002, A&A, 388, 632
Persson C. M. et al., 2018, A&A, 618, A33
Petigura E. A. et al., 2022, AJ, 163, 179
Piaulet C. et al., 2022, Nat. Astron.
Pietrinferni A. et al., 2021, ApJ, 908, 102
Piskunov N., Valenti J. A., 2017, A&A, 597, A16
Pollacco D. L. et al., 2006, PASP, 118, 1407
Rajpaul V., Aigrain S., Osborne M. A., Reece S., Roberts S. J., 2015, MNRAS, 452, 2269
Rasmussen C. E., Williams C. K. I., 2005, Gaussian Processes for Machine Learning (Adaptive Computation and Machine Learning). The MIT Press, Cambridge, Massachusetts
Ricker G. R. et al., 2014, J. Astron. Telesc. Instrum. Syst., 1, 014003
Rogers J. G., Schlichting H. E., Owen J. E., 2023, ApJ, 947, L19
Ryabchikova T., Piskunov N., Kurucz R. L., Stempels H. C., Heiter U., Pakhomov Y., Barklem P. S., 2015, Phys. Scr., 90, 054005
Salvatier J., Wiecki T. V., Fonnesbeck C., 2016, PeerJ Comput. Sci., 2, e55
Serenelli A. M., Bergemann M., Ruchti G., Casagrande L., 2013, MNRAS, 429, 3645
Serrano L. M. et al., 2022, Nat. Astron., 6, 736
Silva Aguirre V. et al., 2015, MNRAS, 452, 2127
Stassun K. G. et al., 2019, AJ, 158, 138
Steffen J. H., 2016, MNRAS, 457, 4384
Twicken J. et al., 2019, in American Astronomical Society Meeting Abstracts #233. p. 140.03
Valenti J. A., Piskunov N., 1996, A&AS, 118, 595
Van Eylen V., Agentoft C., Lundkvist M. S., Kjeldsen H., Owen J. E., Fulton B. J., Petigura E., Snellen I., 2018, MNRAS, 479, 4786
Van Eylen V. et al., 2021, MNRAS, 507, 2154
Vines J. I., Jenkins J. S., 2022, MNRAS, 513, 2719
Yee S. W., Petigura E. A., von Braun K., 2017, ApJ, 836, 77
Zechmeister M., Kürster M., 2009, A&A, 496, 577
Zechmeister M. et al., 2018, A&A, 609, A12
Zeng L. et al., 2019, Proc. Natl. Acad. Sci. USA, 116, 9723
Zeng L. et al., 2021, ApJ, 923, 247

APPENDIX A: APPENDIX

Table A1. Absolute radial velocities and spectral activity indicators measured from the HARPS spectra with the DRS.

BJD_{TBD} −2450000	RV ($km\,s^{-1}$)	σ_{RV} ($km\,s^{-1}$)	FWHM ($km\,s^{-1}$)	BIS ($km\,s^{-1}$)	Contrast (per cent)	T_{exp} (s)	SNR @550nm
8578.51514	8.3561	0.0035	6.5993	0.0833	38.785	1800	35.5
8579.53150	8.3449	0.0030	6.6112	0.0635	38.743	1500	40.8
9205.63053	8.3640	0.0026	6.4372	0.0499	39.787	1800	43.0
9206.63247	8.3729	0.0018	6.4598	0.0446	39.642	1800	58.6
9207.57568	8.3665	0.0022	6.4685	0.0398	39.526	1800	48.5
9207.66046	8.3655	0.0018	6.4766	0.0470	39.529	1800	58.1
9214.71815	8.3418	0.0019	6.4361	0.0721	39.454	2400	57.0
9215.64475	8.3462	0.0017	6.4391	0.0708	39.640	2400	62.0
9217.68640	8.3486	0.0019	6.4223	0.0515	39.845	1800	55.1
9218.68225	8.3483	0.0017	6.4289	0.0527	39.817	1800	61.0
9219.65704	8.3470	0.0016	6.4178	0.0542	39.848	1800	64.6
9221.60896	8.3482	0.0017	6.4250	0.0660	39.860	1800	60.8
9222.61015	8.3382	0.0016	6.4123	0.0583	39.892	1800	64.0
9223.56895	8.3505	0.0017	6.4189	0.0525	39.943	1800	60.7
9224.66129	8.3476	0.0018	6.4348	0.0403	39.820	1800	58.5
9226.65544	8.3572	0.0019	6.4612	0.0390	39.638	1800	56.1
9227.66789	8.3493	0.0023	6.4623	0.0571	39.592	1800	46.5
9228.64010	8.3423	0.0028	6.4661	0.0659	39.562	1800	40.5
9230.63045	8.3425	0.0017	6.4496	0.0663	39.652	1800	61.3
9231.63611	8.3439	0.0025	6.4623	0.0673	39.691	1800	44.2
9232.63467	8.3486	0.0016	6.4501	0.0619	39.705	1800	64.8
9233.67770	8.3443	0.0018	6.4614	0.0573	39.736	1800	59.0
9242.62501	8.3451	0.0016	6.4328	0.0650	39.495	2400	67.8
9243.56834	8.3522	0.0017	6.4395	0.0521	39.540	1800	62.0
9244.54494	8.3552	0.0019	6.4387	0.0528	39.538	1800	55.9
9244.62785	8.3553	0.0017	6.4513	0.0519	39.516	1800	63.9
9245.60955	8.3526	0.0027	6.4711	0.0454	39.245	1800	41.7
9246.63208	8.3594	0.0020	6.4711	0.0625	39.388	1800	53.8
9247.59527	8.3478	0.0021	6.4614	0.0628	39.417	1800	50.9
9248.61373	8.3503	0.0032	6.4636	0.0792	39.252	2700	36.4
9249.62657	8.3502	0.0022	6.4572	0.0698	39.648	2100	49.9
9250.57953	8.3420	0.0027	6.4415	0.0538	39.744	1860	42.2
9251.59236	8.3586	0.0026	6.4425	0.0492	39.694	1800	43.7
9256.62889	8.3508	0.0021	6.4400	0.0542	39.724	1800	53.8
9257.58116	8.3564	0.0017	6.4369	0.0595	39.724	1800	64.6
9261.63836	8.3525	0.0031	6.4272	0.0582	39.488	1800	38.4
9262.59334	8.3549	0.0028	6.4447	0.0652	39.466	1800	41.8
9264.60899	8.3479	0.0019	6.4604	0.0502	39.435	1800	59.2
9265.56638	8.3532	0.0019	6.4639	0.0633	39.396	1800	57.8
9266.55658	8.3535	0.0022	6.4603	0.0633	39.334	1800	50.4
9267.55362	8.3425	0.0020	6.4707	0.0640	39.352	1800	55.6
9269.57020	8.3487	0.0024	6.4821	0.0541	39.077	1800	47.9
9272.57672	8.3419	0.0021	6.4640	0.0555	39.208	1800	55.5
9273.59284	8.3397	0.0034	6.4738	0.0650	38.892	1800	37.2
9274.58962	8.3417	0.0022	6.5579	0.0610	38.735	1800	52.0
9275.56486	8.3413	0.0023	6.5514	0.0540	38.866	1800	49.6
9276.59246	8.3501	0.0026	6.5467	0.0656	38.799	1800	45.8
9277.57256	8.3518	0.0024	6.5421	0.0557	38.822	1800	48.9
9284.57306	8.3475	0.0024	6.5636	0.0653	38.916	1800	48.1
9287.53172	8.3509	0.0021	6.5785	0.0534	38.835	1800	54.6
9288.53857	8.3512	0.0022	6.5767	0.0612	38.844	1800	51.3
9290.53613	8.3509	0.0024	6.5842	0.0594	38.662	1800	48.7

Table A1 – *continued*

BJD_{TBD} −2450000	RV ($km\,s^{-1}$)	σ_{RV} ($km\,s^{-1}$)	FWHM ($km\,s^{-1}$)	BIS ($km\,s^{-1}$)	Contrast (per cent)	T_{exp} (s)	SNR @550nm
9291.52201	8.3473	0.0019	6.6084	0.0724	38.602	1800	58.6
9294.53123	8.3411	0.0042	6.4445	0.0656	39.689	1800	31.0
9295.53344	8.3511	0.0021	6.5290	0.0583	39.035	2100	52.6
9296.51173	8.3565	0.0018	6.5513	0.0555	38.968	1800	61.4
9297.52848	8.3549	0.0019	6.5676	0.0610	38.844	1800	60.2
9490.84461	8.3381	0.0031	6.4877	0.0455	39.551	2100	35.6
9491.81716	8.3320	0.0034	6.4756	0.0611	39.570	2100	33.3
9497.84874	8.3623	0.0024	6.5573	0.0357	39.088	2100	45.0
9501.84420	8.3521	0.0028	6.6205	0.0841	38.682	2100	41.3
9502.76982	8.3440	0.0021	6.5560	0.0797	38.988	2100	50.3
9503.79777	8.3469	0.0033	6.5105	0.0817	39.296	2100	34.5
9504.76620	8.3426	0.0019	6.5036	0.0798	39.304	2100	52.6
9505.77836	8.3443	0.0020	6.4825	0.0727	39.424	2100	51.7
9506.76111	8.3513	0.0019	6.4833	0.0532	39.397	2100	51.5
9515.84526	8.3553	0.0020	6.4251	0.0505	39.651	2100	51.8
9520.79982	8.3479	0.0022	6.5727	0.0768	38.986	2100	47.8
9521.83149	8.3351	0.0027	6.5614	0.0698	39.099	1800	40.8
9528.73056	8.3472	0.0016	6.4964	0.0595	39.430	2100	61.4
9529.73908	8.3359	0.0015	6.3965	0.0611	40.033	2100	66.8
9530.74356	8.3309	0.0017	6.4914	0.0694	39.560	2100	57.6
9531.71638	8.3378	0.0016	6.3912	0.0595	40.061	2100	63.7
9543.61494	8.3315	0.0034	6.4788	0.0713	39.594	2100	33.3
9545.68951	8.3502	0.0027	6.4897	0.0612	39.545	2100	39.4
9546.72099	8.3539	0.0022	6.4835	0.0458	39.584	2100	47.8
9547.69656	8.3478	0.0016	6.5002	0.0518	39.420	2100	61.0
9548.80186	8.3506	0.0016	6.5131	0.0586	39.395	2100	62.6
9550.71766	8.3409	0.0039	6.5141	0.0607	39.461	1800	30.9
9560.66602	8.3452	0.0017	6.5592	0.0726	39.081	2100	59.0
9561.67646	8.3432	0.0029	6.5259	0.0777	39.188	2100	38.7
9563.68304	8.3437	0.0018	6.5071	0.0648	39.222	2100	57.8
9564.66694	8.3414	0.0021	6.5121	0.0508	39.162	2100	50.6
9577.74753	8.3495	0.0016	6.6025	0.0607	38.779	2100	62.9
9579.75033	8.3417	0.0019	6.5518	0.0774	39.066	2100	53.9
9581.72990	8.3445	0.0017	6.5317	0.0701	39.188	2100	59.1
9583.70601	8.3418	0.0019	6.5170	0.0536	39.369	2100	53.7
9584.59477	8.3422	0.0015	6.4280	0.0693	39.868	2100	67.8
9584.72285	8.3367	0.0017	6.5352	0.0527	39.275	2100	60.9
9585.58600	8.3453	0.0019	6.5261	0.0634	39.290	2100	54.7
9585.72824	8.3452	0.0018	6.5310	0.0657	39.298	2100	57.8
9586.72537	8.3349	0.0020	6.5147	0.0628	39.340	2100	52.4
9587.72124	8.3372	0.0020	6.5399	0.0621	39.176	1800	52.8
9588.56786	8.3388	0.0017	6.4888	0.0641	39.473	2100	59.8
9588.71681	8.3391	0.0020	6.5125	0.0550	39.362	1800	52.0
9589.71870	8.3407	0.0027	6.5096	0.0609	39.411	1808	41.6
9590.59269	8.3467	0.0025	6.5111	0.0596	39.275	2100	44.3
9591.58055	8.3421	0.0014	6.5012	0.0467	39.353	2100	71.9
9591.73732	8.3422	0.0030	6.5125	0.0577	39.195	2100	38.8
9592.59389	8.3501	0.0014	6.5164	0.0463	39.230	2100	69.1
9592.72732	8.3519	0.0021	6.5372	0.0396	38.925	2100	51.1
9606.67799	8.3471	0.0023	6.4959	0.0590	39.498	2100	46.8
9609.64815	8.3498	0.0015	6.5043	0.0614	39.329	2100	68.4
9610.65838	8.3519	0.0017	6.5121	0.0556	39.229	2100	62.5
9626.55046	8.3360	0.0019	6.5169	0.0653	39.220	2100	54.6
9627.55019	8.3415	0.0021	6.4967	0.0683	39.226	2100	49.5
9628.54583	8.3358	0.0017	6.4972	0.0659	39.329	2100	58.1
9629.56926	8.3376	0.0016	6.5055	0.0595	39.418	2100	59.9

Table A2. Relative radial velocities and spectral activity indicators measured from the HARPS spectra with SERVAL and TERRA.

BJD_{TBD} -2450000	RV ($km\,s^{-1}$)	σ_{RV} ($km\,s^{-1}$)	dlW ($km\,s^{-1}\,Np^{-1}$)	σ_{dlW} ($km\,s^{-1}\,Np^{-1}$)	CRX ($m^2\,s^{-2}$)	σ_{CRX} ($m^2\,s^{-2}$)	S-index –	$\sigma_{S\text{-}index}$ –	H_α –	Na D_1 –	Na D_2 –
8578.51514	0.0032	0.0026	34.208	3.675	8.059	23.737	1.287	0.018	0.432	1.219	0.968
8579.53150	−0.0034	0.0021	32.141	2.956	3.908	19.040	1.202	0.016	0.473	1.220	0.965
9205.63053	0.0194	0.0017	1.408	2.658	1.540	14.505	1.172	0.013	0.480	1.244	1.004
9206.63247	0.0304	0.0014	7.962	1.862	−1.187	12.339	1.126	0.010	0.501	1.239	0.988
9207.57568	0.0215	0.0019	14.317	2.154	11.742	16.447	1.150	0.012	0.477	1.241	0.978
9207.66046	0.0227	0.0013	18.549	1.854	−6.042	11.509	1.157	0.011	0.477	1.241	0.979
9214.71815	−0.0021	0.0014	16.143	1.665	7.481	11.826	1.098	0.011	0.496	1.240	0.990
9215.64475	0.0003	0.0012	7.563	1.671	3.814	10.529	1.094	0.009	0.505	1.243	0.990
9217.68640	0.0025	0.0013	−6.021	1.627	−3.028	11.113	1.119	0.011	0.497	1.243	0.996
9218.68225	0.0052	0.0016	−0.511	1.910	−16.867	13.649	1.117	0.010	0.505	1.248	0.995
9219.65704	0.0017	0.0011	−2.072	1.314	−7.816	9.266	1.178	0.010	0.511	1.245	0.994
9221.60896	0.0009	0.0021	−9.785	1.701	−11.633	18.359	1.061	0.010	0.524	1.247	0.998
9222.61015	−0.0022	0.0012	−9.937	1.485	1.309	10.524	1.078	0.009	0.513	1.255	0.997
9223.56895	0.0063	0.0016	−13.314	1.676	5.411	13.658	1.067	0.009	0.513	1.247	0.993
9224.66129	0.0076	0.0015	−8.005	1.551	8.850	12.633	1.125	0.011	0.496	1.248	1.001
9226.65544	0.0177	0.0018	15.761	1.684	−6.285	15.531	1.202	0.012	0.462	1.245	0.995
9227.66789	0.0076	0.0016	16.473	2.468	13.923	14.013	1.158	0.013	0.485	1.232	0.989
9228.64010	−0.0037	0.0018	21.783	2.357	14.554	15.479	1.222	0.014	0.460	1.232	0.999
9230.63045	−0.0030	0.0015	11.931	1.842	1.778	13.448	1.205	0.010	0.463	1.237	0.996
9231.63611	−0.0016	0.0018	5.839	2.627	4.030	15.996	1.227	0.013	0.437	1.241	0.983
9232.63467	0.0054	0.0014	6.978	1.499	2.628	12.142	1.148	0.009	0.508	1.246	0.979
9233.67770	−0.0010	0.0012	6.140	1.694	−5.641	10.425	1.227	0.011	0.499	1.248	0.980
9242.62501	0.0035	0.0011	1.181	1.876	1.219	9.600	1.110	0.009	0.473	1.248	0.988
9243.56834	0.0084	0.0016	2.409	1.752	24.240	13.777	1.042	0.009	0.500	1.249	0.997
9244.54494	0.0136	0.0014	5.752	1.937	−17.013	12.236	1.167	0.010	0.463	1.242	0.988
9244.62785	0.0105	0.0013	6.332	1.635	−17.780	11.490	1.130	0.010	0.481	1.245	0.993
9245.60955	0.0101	0.0022	17.823	2.499	−8.225	19.301	1.085	0.012	0.481	1.241	0.985
9246.63208	0.0176	0.0011	17.052	2.235	14.530	9.895	1.151	0.011	0.476	1.241	0.986
9247.59527	0.0067	0.0014	11.328	2.117	4.072	12.566	1.266	0.012	0.428	1.241	0.990
9248.61373	0.0059	0.0021	16.507	3.031	2.775	18.452	1.107	0.013	0.472	1.241	1.006
9249.62657	0.0061	0.0014	5.621	2.045	−0.665	12.126	1.225	0.012	0.434	1.237	0.989
9250.57953	0.0032	0.0020	2.527	2.567	−29.112	17.551	1.175	0.014	0.486	1.248	0.986
9251.59236	0.0169	0.0018	6.505	2.333	32.852	15.445	1.122	0.013	0.483	1.242	0.987
9256.62889	0.0116	0.0015	-1.067	1.991	20.526	13.127	1.126	0.012	0.510	1.254	0.989
9257.58116	0.0108	0.0012	-0.888	1.812	−3.710	10.565	1.080	0.010	0.514	1.249	0.997
9261.63836	0.0108	0.0020	1.164	2.689	−5.115	17.970	1.179	0.014	0.468	1.242	0.994
9262.59334	0.0086	0.0019	5.578	2.697	−1.354	16.608	1.136	0.013	0.484	1.245	0.991
9264.60899	0.0085	0.0015	12.321	1.688	23.788	13.227	1.141	0.011	0.475	1.243	0.989
9265.56638	0.0105	0.0014	16.936	1.789	13.431	12.501	1.144	0.010	0.479	1.240	0.996
9266.55658	0.0061	0.0016	21.902	2.065	−15.066	14.264	1.058	0.011	0.479	1.227	0.988
9267.55362	−0.0023	0.0017	19.330	2.024	−23.256	14.982	1.128	0.010	0.466	1.236	0.992
9269.57020	0.0036	0.0021	26.274	2.322	−13.285	18.773	1.109	0.012	0.469	1.233	0.996
9272.57672	−0.0034	0.0017	20.085	2.112	−25.857	14.051	1.023	0.011	0.481	1.245	0.988
9273.59284	−0.0062	0.0023	21.943	3.283	28.042	19.846	1.157	0.015	0.479	1.233	0.991
9274.58962	−0.0029	0.0018	14.123	1.905	4.171	15.381	1.048	0.012	0.482	1.246	0.987
9275.56486	−0.0019	0.0019	5.611	2.094	−9.529	16.267	1.098	0.012	0.509	1.248	0.996
9276.59246	0.0045	0.0020	8.596	2.098	−36.640	16.241	1.099	0.013	0.507	1.238	0.991
9277.57256	0.0101	0.0018	5.113	2.221	8.146	14.986	1.077	0.013	0.522	1.255	0.987
9284.57306	0.0012	0.0016	6.835	2.262	16.514	13.827	1.122	0.014	0.490	1.243	0.983
9287.53172	0.0040	0.0016	8.554	2.338	−11.277	13.664	1.219	0.013	0.451	1.240	0.980
9288.53857	0.0059	0.0019	7.805	2.324	23.854	16.430	1.196	0.014	0.465	1.237	0.980
9290.53613	0.0044	0.0021	13.845	2.513	3.938	18.318	1.137	0.013	0.471	1.236	0.982
9291.52201	−0.0008	0.0017	15.065	1.888	−11.754	14.296	1.106	0.012	0.463	1.233	0.984
9294.53123	0.0016	0.0028	5.710	3.835	−40.164	23.510	1.086	0.019	0.489	1.226	0.989
9295.53344	0.0084	0.0016	−3.504	2.134	−18.821	13.893	1.085	0.012	0.489	1.236	0.986
9296.51173	0.0115	0.0014	−5.641	1.553	−25.846	11.635	1.036	0.011	0.491	1.242	0.992
9297.52848	0.0097	0.0015	1.038	1.929	−10.220	12.634	1.080	0.012	0.497	1.241	0.999
9490.84461	−0.0025	0.0021	−10.560	2.627	31.414	17.347	1.017	0.015	0.494	1.239	1.000
9491.81716	−0.0053	0.0024	−9.314	3.564	−1.185	19.828	1.094	0.016	0.504	1.240	0.994
9497.84874	0.0223	0.0018	16.723	2.395	11.851	14.785	1.123	0.013	0.477	1.227	0.991
9501.84420	0.0081	0.0021	35.467	3.039	24.537	17.057	1.212	0.017	0.456	1.232	0.985
9502.76982	−0.0033	0.0018	25.389	2.206	−35.382	14.474	1.137	0.011	0.472	1.236	0.992
9503.79777	0.0049	0.0021	16.456	2.838	12.757	17.890	1.167	0.015	0.482	1.226	0.997

Table A2 – *continued*

BJD_{TBD} −2450000	RV ($km\,s^{-1}$)	σ_{RV} ($km\,s^{-1}$)	dlW ($km\,s^{-1}\,Np^{-1}$)	σ_{dlW} ($km\,s^{-1}\,Np^{-1}$)	CRX ($m^2\,s^{-2}$)	σ_{CRX} ($m^2\,s^{-2}$)	S-index –	$\sigma_{S\text{-}index}$ –	H_α –	Na D_1 –	Na D_2 –
9504.76620	−0.0028	0.0015	1.115	2.058	−5.004	12.200	1.124	0.011	0.510	1.237	0.995
9505.77836	0.0011	0.0013	−8.146	2.128	−3.565	10.689	1.085	0.011	0.500	1.240	0.996
9506.76111	0.0124	0.0015	−7.221	2.400	−4.195	12.763	1.036	0.010	0.505	1.243	0.996
9515.84526	0.0169	0.0012	4.103	1.865	15.499	9.970	1.200	0.011	0.465	1.239	0.996
9520.79982	0.0049	0.0018	26.476	2.408	12.793	15.120	1.218	0.013	0.457	1.224	0.982
9521.83149	−0.0106	0.0023	20.910	2.396	−35.168	18.976	1.140	0.014	0.476	1.233	0.995
9528.73056	0.0038	0.0015	−16.502	1.675	9.057	12.269	1.063	0.010	0.510	1.248	1.006
9529.73908	−0.0047	0.0013	−15.958	1.503	10.040	10.958	1.087	0.009	0.500	1.246	1.000
9530.74356	−0.0128	0.0017	−19.460	1.694	12.450	13.925	0.985	0.010	0.528	1.247	1.006
9531.71638	−0.0043	0.0014	−22.994	1.857	2.905	11.465	1.051	0.009	0.506	1.253	1.009
9543.61494	−0.0062	0.0024	−11.499	2.915	60.551	18.773	1.194	0.017	0.494	1.242	0.995
9545.68951	0.0055	0.0018	−20.699	2.894	−0.357	14.722	1.038	0.013	0.507	1.233	0.997
9546.72099	0.0115	0.0021	−15.993	2.055	−3.592	17.166	1.119	0.012	0.501	1.249	0.999
9547.69656	0.0048	0.0013	−12.159	1.600	18.692	10.477	1.056	0.010	0.513	1.254	1.005
9548.80186	0.0075	0.0012	−13.524	1.677	−3.601	10.365	1.074	0.010	0.511	1.247	1.002
9550.71766	0.0012	0.0022	−15.334	3.639	44.748	17.984	0.987	0.019	0.503	1.250	1.008
9560.66602	0.0024	0.0015	15.928	1.898	−9.347	12.644	1.198	0.010	0.461	1.232	0.990
9561.67646	−0.0012	0.0020	10.411	2.569	24.920	16.595	1.247	0.015	0.454	1.239	0.983
9563.68304	−0.0004	0.0017	−1.442	1.830	7.718	14.258	1.116	0.010	0.503	1.243	0.995
9564.66694	0.0001	0.0015	−4.118	2.391	−14.148	12.000	1.086	0.011	0.498	1.245	1.004
9577.74753	0.0035	0.0012	27.385	1.986	8.929	9.896	1.255	0.012	0.452	1.231	0.982
9579.75033	−0.0033	0.0016	11.216	1.902	13.664	13.375	1.227	0.012	0.476	1.238	0.993
9581.72990	0.0017	0.0015	−5.253	1.439	−4.690	12.474	1.125	0.011	0.514	1.246	0.989
9583.70601	−0.0013	0.0016	−6.852	1.771	5.427	13.540	1.108	0.011	0.500	1.247	0.996
9584.59477	0.0000	0.0010	−7.261	1.347	−3.137	8.676	1.123	0.009	0.498	1.246	0.997
9584.72285	−0.0048	0.0014	−8.671	1.472	−3.113	11.580	1.119	0.010	0.503	1.245	0.993
9585.58600	0.0011	0.0018	−8.802	1.801	−27.674	14.346	1.117	0.011	0.509	1.242	0.996
9585.72824	−0.0002	0.0014	−8.467	1.504	20.429	11.416	1.060	0.011	0.519	1.247	0.991
9586.72537	−0.0066	0.0014	−9.467	2.168	−16.669	11.553	1.087	0.012	0.502	1.243	0.993
9587.72124	−0.0044	0.0019	−15.800	1.706	19.157	15.762	1.036	0.013	0.532	1.252	0.997
9588.56786	−0.0024	0.0012	−15.175	1.775	−10.650	9.543	1.043	0.009	0.526	1.251	0.995
9588.71681	−0.0035	0.0013	−18.477	1.962	−9.275	10.962	1.024	0.012	0.546	1.254	0.995
9589.71870	−0.0024	0.0020	−22.861	3.204	9.360	17.309	0.963	0.015	0.556	1.259	0.980
9590.59269	0.0045	0.0018	−16.850	2.585	−20.246	15.141	1.009	0.014	0.553	1.254	0.980
9591.58055	−0.0001	0.0012	−17.048	1.674	−10.154	9.889	1.052	0.009	0.545	1.257	0.968
9591.73732	0.0042	0.0021	−19.114	3.110	20.262	17.930	1.027	0.017	0.558	1.259	0.957
9592.59389	0.0097	0.0014	−9.301	1.424	12.005	11.847	1.055	0.009	0.540	1.255	0.971
9592.72732	0.0102	0.0017	−1.401	2.003	13.551	14.051	1.091	0.013	0.554	1.259	0.962
9606.67799	0.0067	0.0021	−20.079	2.204	−9.169	17.897	1.074	0.013	0.514	1.250	0.994
9609.64815	0.0041	0.0011	−21.853	1.758	4.793	8.854	1.100	0.009	0.489	1.251	1.005
9610.65838	0.0077	0.0015	−19.701	2.086	1.889	12.824	1.070	0.010	0.521	1.257	0.994
9626.55046	−0.0051	0.0014	−4.369	1.641	4.147	11.515	1.048	0.011	0.515	1.248	1.001
9627.55019	−0.0022	0.0017	−1.363	2.395	31.082	13.849	1.091	0.011	0.495	1.249	0.999
9628.54583	−0.0063	0.0014	−12.073	1.657	−24.609	11.074	1.065	0.010	0.518	1.246	1.005
9629.56926	−0.0043	0.0015	−17.272	1.985	−17.906	12.741	1.092	0.010	0.512	1.253	1.002

Table A3. Absolute radial velocities and spectral activity indicators measured from the HARPS-N spectra with the DRS.

BJD_{TBD} −2450000	RV ($km\,s^{-1}$)	σ_{RV} ($km\,s^{-1}$)	FWHM ($km\,s^{-1}$)	BIS ($km\,s^{-1}$)	Contrast (per cent)	T_{exp} (s)	SNR @550nm
8578.35923	8.3519	0.0019	6.5098	0.0696	39.407	2400	51.6
8579.35283	8.3376	0.0048	6.4946	0.0508	39.360	1230	25.1
8732.71766	8.3678	0.0052	6.4912	0.0487	39.276	1800	23.1
8732.74144	8.3591	0.0064	6.5139	0.0486	39.264	1800	19.8
8752.68369	8.3692	0.0017	6.4828	0.0564	39.660	1800	57.7
8752.70581	8.3665	0.0014	6.4835	0.0600	39.669	1800	67.4
8753.70744	8.3513	0.0021	6.4844	0.0657	39.616	1800	47.3
8754.71549	8.3551	0.0017	6.4857	0.0632	39.663	1800	55.7
9204.51620	8.3541	0.0023	6.4273	0.0419	39.997	1800	42.4
9204.65656	8.3560	0.0018	6.4217	0.0470	40.037	1800	52.0
9205.54599	8.3619	0.0015	6.4309	0.0386	40.037	1500	60.1
9205.63930	8.3590	0.0014	6.4366	0.0510	40.001	1500	65.9
9206.47971	8.3674	0.0018	6.4567	0.0291	39.875	1800	52.3
9206.65731	8.3705	0.0019	6.4491	0.0362	39.874	2400	51.4

Table A4. Relative radial velocities and spectral activity indicators measured from the HARPS-N spectra with SERVAL and TERRA.

BJD_{TBD} −2450000	RV ($km\,s^{-1}$)	σ_{RV} ($km\,s^{-1}$)	dlW ($km\,s^{-1}\,Np^{-1}$)	σ_{dlW} ($km\,s^{-1}\,Np^{-1}$)	CRX ($m^2\,s^{-2}$)	σ_{CRX} ($m^2\,s^{-2}$)	S-index –	$\sigma_{S\text{-}index}$ –	H_α –	Na D_1 –	Na D_2 –
8578.35923	−0.0153	0.0012	−10.331	3.298	−14.213	10.557	1.289	0.010	0.382	1.2058	0.9705
8579.35283	−0.0189	0.0023	−2.017	4.584	−4.860	20.180	1.099	0.018	0.407	1.2022	0.9588
8732.71766	0.0062	0.0025	−0.417	5.610	−35.894	20.131	1.477	0.022	0.368	1.1750	0.9311
8732.74144	−0.0029	0.0033	−6.190	5.519	−23.484	28.098	1.482	0.025	0.374	1.1705	0.9313
8752.68369	0.0004	0.0010	−24.896	2.236	1.003	8.720	1.216	0.009	0.416	1.2200	0.9864
8752.70581	0.0001	0.0009	−27.621	2.072	9.871	7.201	1.208	0.007	0.412	1.2189	0.9840
8753.70744	−0.0153	0.0012	−22.886	2.317	−4.919	10.278	1.217	0.010	0.411	1.2071	0.9789
8754.71549	−0.0119	0.0011	−31.619	2.284	−11.948	9.137	1.264	0.009	0.396	1.2214	0.9830
9204.51620	−0.0115	0.0016	−57.931	2.722	30.076	13.728	1.144	0.011	0.461	1.2207	0.9819
9204.65656	−0.0069	0.0011	−62.660	2.495	−8.303	9.456	1.153	0.009	0.451	1.2261	0.9966
9205.54599	−0.0019	0.0011	−58.627	2.216	13.321	9.308	1.159	0.007	0.434	1.2321	0.9950
9205.63930	−0.0044	0.0010	−58.836	1.951	4.622	8.335	1.167	0.007	0.442	1.2318	0.9930
9206.47971	0.0017	0.0012	−47.854	2.351	−2.439	11.255	1.144	0.008	0.451	1.2231	0.9867
9206.65731	0.0022	0.0012	−44.826	2.328	−11.085	9.886	1.133	0.009	0.446	1.2166	0.9821

Table A5. Comparison of all RV fitting models used, all results are within 1-sigma.

Toolkit	GP kernel	Activity indicator	Number of planets	Eccentricity	K_b (m s^{-1})	M_b ($M_\oplus$)
RadVel	No GP	–	2	Circular	$2.77^{+0.81}_{-0.82}$	$3.69^{+1.19}_{1.14}$
RadVel	Celerite quasi-periodic	–	1	Circular	2.61 ± 0.49	$3.48^{+0.73}_{0.70}$
RadVel	Celerite quasi-periodic	–	2	Circular	$2.59^{+0.49}_{-0.48}$	$3.45^{+0.73}_{0.71}$
RadVel	Celerite quasi-periodic	–	2	Both eccentric	$3.22^{+1.9}_{-0.69}$	$4.29^{+2.66}_{0.98}$
RadVel	Celerite quasi-periodic	–	3	Circular	2.60 ± 0.50	$3.46^{+0.74}_{0.72}$
RadVel HARPS only	Celerite quasi-periodic	–	2	Circular	2.83 ± 0.53	$3.77^{+0.79}_{0.76}$
RadVel	Square exponential	–	2	Circular	2.70 ± 0.40	$3.59^{+0.61}_{0.59}$
RadVel	Square exponential	–	2	Outer planet eccentric	$2.69^{+0.37}_{-0.36}$	$3.58^{+0.57}_{0.55}$
RadVel	Square exponential	–	3	Circular	$2.67^{+0.39}_{-0.40}$	$3.55^{+0.61}_{0.59}$
Pyaneti multi-dimensional	Quasi-periodic	S-index	2	Circular	2.07 ± 0.39	2.75 ± 0.52
Pyaneti multi-dimensional	Quasi-periodic	S-index	2	Both eccentric	$2.66^{+0.44}_{-0.41}$	3.28 ± 0.48
Pyaneti multi-dimensional	Quasi-periodic	S-index	2	Outer planet eccentric	2.17 ± 0.36	2.89 ± 0.48
Pyaneti multi-dimensional	Quasi-periodic	Contrast	2	Both eccentric	$2.47^{+0.41}_{-0.40}$	3.13 ± 0.49
Pyaneti multi-dimensional	Quasi-periodic	FWHM	2	Both eccentric	$2.48^{+0.38}_{-0.37}$	3.16 ± 0.47
Pyaneti multi-dimensional	Quasi-periodic	S-index & FWHM	2	Both eccentric	$2.56^{+0.43}_{-0.39}$	$3.20^{+0.48}_{-0.47}$
Pyaneti multi-dimensional	Quasi-periodic	S-index & contrast	2	Both eccentric	$2.59^{+0.42}_{-0.40}$	$3.22^{+0.48}_{-0.46}$
Pyaneti multi-dimensional	Quasi-periodic	FWHM & contrast	2	Both eccentric	$2.55^{+0.46}_{-0.43}$	$3.26^{+0.57}_{-0.55}$
Pyaneti RV only	Quasi-periodic	–	2	Both eccentric	$2.52^{+0.40}_{-0.38}$	$3.16^{+0.46}_{-0.47}$
Pyaneti RV only	Quasi-periodic	–	2	Outer planet eccentric	2.12 ± 0.35	$2.82^{+0.48}_{-0.47}$
Pyaneti joint model	Quasi-periodic	S-index	2	Both eccentric	2.58 ± 0.38	$3.28^{+0.47}_{-0.48}$

Table A6. Priors used for the RV fitting for each parameter. $\mathcal{U}$[a,b] refers to uniform priors in the range a – b, $\mathcal{N}$[a,b] refers to a Gaussian prior with mean a and width b, and $\mathcal{F}$[a,b] is a fixed parameter at value a.

Fitted parameter	Prior
Planet parameters	
Orbital period, P_b (d)	$\mathcal{N}$[1.5484, 0.000002]
Time of inf. conjunction, $T_{conj,b}$ (BJD_{TDB})	$\mathcal{N}$[2459199.0314, 0.0007]
RV amplitude, K_b (km s^{-1})	$\mathcal{U}$[0.0000, 0.0500]
$ew1_b$, $\sqrt{e_b}\sin\omega_b$	$\mathcal{F}$[0.0000, 0.0000]
$ew2_b$, $\sqrt{e_b}\cos\omega_b$	$\mathcal{F}$[0.0000, 0.0000]
Orbital period, P_c (d)	$\mathcal{U}$[49.0000, 52.0000]
Time of inf. conjunction, $T_{conj,c}$ (BJD_{TDB})	$\mathcal{U}$[2459205.0000, 2459225.0000]
RV amplitude, K_c (km s^{-1})	$\mathcal{U}$[0.0000, 0.0500]
$ew1_c$, $\sqrt{e_c}\sin\omega_c$	$\mathcal{U}$[−1.0000, 1.0000]
$ew2_c$, $\sqrt{e_c}\cos\omega_c$	$\mathcal{U}$[−1.0000, 1.0000]
Other parameters	
GP hyperparameters	
A_0	$\mathcal{U}$[0.0, 0.05]
A_1	$\mathcal{U}$[0.0, 0.1]
A_2	$\mathcal{U}$[0., 0.25]
A_3	$\equiv 0$
λ_e (d)	$\mathcal{U}$[1, 500]
λ_p	$\mathcal{U}$[0.1, 3.0]
Rotation period, P_{GP} (d)	$\mathcal{U}$[15.0, 25.0]

Table A7. Priors used for the transit fitting for each parameter. $\mathcal{U}$[a,b] refers to uniform priors in the range a – b, $\mathcal{N}$[a,b] refers to a Gaussian prior with mean a and width b, and $\mathcal{F}$[a,b] is a fixed parameter at value a.

Fitted parameter	Prior
Planet parameters	
Orbital period, P_b (d)	$\mathcal{U}$[1.547352, 1.549352]
Time of mid-transit, T_0 (BJD_{TDB})	$\mathcal{U}$[2459199.02185, 2459199.041850]
$R_b/R_\star$	$\mathcal{U}$[0.023699, 0.039530]
Impact parameter b	$\mathcal{U}$[0, 1]
Other parameters	
$M_\star$ ($M_\odot$)	$\mathcal{N}$[0.630, 0.018]
$R_\star$ ($R_\odot$)	$\mathcal{N}$[0.624, 0.013]
u_1	$\mathcal{N}$[0.436, 0.202]
u_2	$\mathcal{N}$[0.217, 0.155]
Noise model parameters	
ρ_{GP} (d)	$\mathcal{N}$[10.0, 5.0]
σ_{GP} (ppt)	$\mathcal{N}$[1.0, 0.5]
$\log\sigma_{S6}$ (ppt)	$\mathcal{N}$[−0.614, 10]
$\log\sigma_{S32}$ (ppt)	$\mathcal{N}$[−0.684, 10]

This paper has been typeset from a TEX/LATEX file prepared by the author.